Adaptive stabilization for *Q*-compensated reverse time migration

Yufeng Wang[1], Hui Zhou[1], Hanming Chen[1], and Yangkang Chen[2]

ABSTRACT

Reverse time migration (RTM) for attenuating media should take amplitude compensation and phase correction into consideration. However, attenuation compensation during seismic propagation suffers from numerical instability because of the boosted high-frequency ambient noise. We have developed a novel adaptive stabilization method for *Q*-compensated RTM (*Q*-RTM), which exhibits superior properties of time variance and *Q* dependence over conventional low-pass filtering-based method. We derive the stabilization operator by first analytically deriving *k*-space Green's functions for a constant-*Q* wave equation with decoupled fractional Laplacians and its compensated equation. The time propagator of Green's function for the viscoacoustic wave equation decreases exponentially, whereas that of the compensated equation is exponentially divergent at a high wavenumber, and it is not stable after the wave is extrapolated for a long time. Therefore, the Green's functions theoretically explain how the numerical instability existing in *Q*-RTM arises and shed light on how to overcome this problem pertinently. The stabilization factor required in the proposed method can be explicitly identified by the specified gain limit according to an empirical formula. The *Q*-RTM results for noise-free data using low-pass filtering and adaptive stabilization are compared over a simple five-layer model and the BP gas chimney model to verify the superiority of the proposed approach in terms of fidelity and stability. The *Q*-RTM result for noisy data from the BP gas chimney model further demonstrates that our method enjoys a better antinoise performance and helps significantly to enhance the resolution of seismic images.

INTRODUCTION

When seismic waves travel through the earth subsurface, the absorption and dispersion caused by the anelasticity of the subsurface will inevitably degrade the quality of seismograms, decrease the resolution of migrated images, and eventually affect the reliability of seismic interpretation. These frequency-dependent attenuating effects can be investigated by mathematical modeling (Liu et al., 1976; Carcione et al., 1988), laboratory measurements (Wuenschel, 1965; Wang et al., 2007, 2010), and pulse propagation experiments in the field (McDonal et al., 1958; Li et al., 2016a). It is essential to compensate amplitude loss and phase distortion. In general, attenuation compensation in geophysics can be roughly classified into two categories: seismic record-based compensation and propagation-based compensation. The former category of compensation methods includes time-varying deconvolution (Clarke, 1968; Griffiths et al., 1977; Margrave et al., 2011), time-variant spectral whitening (Yilmaz, 2001), and inverse-*Q* filtering (Hargreaves and Calvert, 1991; Wang, 2002, 2006). All of these processing methods are conducted to directly enhance the resolution of attenuated seismic records in the time domain or frequency domain. Nevertheless, amplitude attenuation and phase dispersion associated with anelasticity occur during the wave propagation, so it is more physically consistent to mitigate these effects in prestack depth migration (Zhang et al., 2010; Zhu et al., 2014). The second category of compensation schemes are performed during seismic propagation, which contains *Q*-compensated one-way wave equation migration (Dai and West, 1994; Mittet et al., 1995; Wang and Guo, 2004; Mittet, 2007; Zhang et al., 2012), *Q*-compensated reverse time migration (*Q*-RTM; Zhang et al., 2010; Zhu et al., 2014; Guo et al., 2016; Li et al., 2016b; Sun et al., 2016; Wang et al., 2017a), and *Q*-compensated Gaussian beam migration (Bai et al., 2016a, 2016b).

In this paper, we focus on Q-RTM using viscoacoustic-wave equation with decoupled fractional Laplacians (DFL), which is first developed by Treeby and Cox (2010) based on power-law absorption and dispersion. This equation has been successfully applied into photoacoustic tomography in medicine (Treeby et al., 2010; Huang et al., 2012). In geophysics, frequency-dependent absorption and dispersion are typically characterized by the constant-Q model (McDonal et al., 1958; Kjartansson, 1979; Carcione et al., 1988), which exhibits a mathematically concise dispersion relation featuring Q exactly independent of frequency. Zhu and Harris (2014) extend DFLs to the constant-Q wave equation. This equation is attractive for Q-RTM partly due to its flexibility for separately compensating absorption and correcting dispersion. Zhu et al. (2014) and Zhu (2014) explain that reversing the sign of the memory variable term of the standard linear solid (SLS) model will not fully compensate for phase dispersion. Guo and Mcmechan (2015) and Guo et al. (2016) further verify the phase dislocation existing in coupled Q-RTM by numerically comparing Q-RTM based on coupled SLS equation with Q-RTM based on the decoupled constant-Q equation. In addition, viscoacoustic-wave equation with DFL relieves memory burden resulted from the temporal nonlocality of fractional time derivatives (Carcione et al., 2002; Carcione, 2008; Wang et al., 2015) because DFL is nonlocal in space rather than in time, and it can be implemented efficiently by Fourier pseudospectral method (PSM) (Carcione, 2010; Sun et al., 2014; Zhu and Carcione, 2014; Chen et al., 2016).

As proposed by Treeby et al. (2010) and Zhu et al. (2014), attenuation compensation based on viscoacoustic-wave equation with DFLs can be easily achieved by reversing the absorption proportionality coefficient in sign but leaving the equivalent dispersion parameter unchanged. However, such an artificial compensation is prone to boost the ambient noise coming from high-frequency noise in seismic data or the machine errors relative to working precision (Wang, 2009; Yang et al., 2016b). Because Green's function can help to understand the numerical performance of the wave equation (Kelly et al., 2008; Treeby and Cox, 2011; Wang et al., 2017c), we derive k-space Green's functions for constant-Q wave equation and its compensated equation. The time propagator of Green's function deduced from the compensated equation is exponential divergent at high wavenumber, and thus makes the propagation-based compensation an ill-posed problem, which theoretically explains the numerical instability existing in Q-RTM.

Now that we have figured out the essential reason resulting in numerical instability during attenuation compensation, reasonable stabilization needs to be incorporated either in the frequency or wavenumber domain (Ammari et al., 2013; Kalimeris and Scherzer, 2013). Because the constant-Q wave equation with DFLs is simulated by PSM in this paper, it is natural to conduct stabilization in the wavenumber domain rather than in the frequency domain. Conventionally, high-frequency ambient noise is suppressed by a low-pass Tukey filter with its cut-off frequency identified by the noise level of measured data (Treeby et al., 2010; Zhu et al., 2014; Li et al., 2016b). However, conventional time-invariant filtering fails to adapt with spatially varying Q and compensation depth (traveltime). Treeby (2013) applies a time-variant frequency domain Tukey window for regularizing compensated photoacoustic tomography, whose cut-off frequency is chosen according to the local time-frequency distribution of the recorded signals. Unlike conventional low-pass filtering acting as a damage controller to suppress

the noise caused by attenuation compensation, the stabilization scheme attempts to find a stable operator for attenuation compensation (Wang and Guo, 2004). Wang and Guo (2004) propose a robust stabilized approach for inverse-Q filtered migration, in which the amplitude-compensation operator is defined by introducing a stabilization factor. In this paper, we develop an adaptive stabilization for Q-RTM, in which the stabilization factor can be explicitly identified by the specified gain limit according to an empirical formula (Wang, 2006). Compensation with adaptive stabilization exhibits superior properties of time variance and Q dependence over conventional low-pass filtering.

This paper is organized as follows: We first describe the methodology of Q-RTM in the framework of constant-Q wave equation with DFLs. Next, we analytically derive k-space Green's functions for constant-Q wave equation and its compensated equation. Based on the exponentially divergent time propagator of Green's function, an adaptive stabilization scheme is therefore developed for Q-RTM. Following that, we investigate the compensation and stabilization effects of our proposed scheme by adopting control variable method and further compare them with those of conventional low-pass filtering. We demonstrate the stability and feasibility of Q-RTM with adaptive stabilization using several synthetic examples with different levels of complexity. Finally, we conduct a discussion and draw some conclusions.

Q-RTM USING THE CONSTANT-Q WAVE EQUATION

General principle of Q-RTM

We first introduce the general principle of Q-RTM in the framework of constant-Q wave equation with DFLs, which is proposed by Zhu and Harris (2014) as follows:

$$\begin{cases} \frac{1}{c^2(\mathbf{x})}\frac{\partial^2 p}{\partial t^2}(\mathbf{x},t) - \eta(\mathbf{x})(-\nabla^2)^{\gamma(\mathbf{x})+1}p(\mathbf{x},t) - \tau(\mathbf{x})\frac{\partial}{\partial t}(-\nabla^2)^{\gamma(\mathbf{x})+1/2}p(\mathbf{x},t) = \delta(\mathbf{x}-\mathbf{x}_s)f(t), \\ p(\mathbf{x},t) = \frac{\partial p}{\partial t}(\mathbf{x},t) = 0, \mathbf{x}\in\Omega, t<0, \end{cases}$$

$$(1)$$

where Ω is a bounded domain in d-dimensional space $\mathbb{R}^d$, $\mathbf{x}_s$ denotes the source position, and $f(t)$ is the point source signature enforced at $\mathbf{x}_s$. The dimensionless parameter $\gamma(\mathbf{x}) = \arctan(1/\pi Q(\mathbf{x}))$ ranges within (0, 1/2), and $c^2(\mathbf{x}) = c_0^2\cos^2(\pi\gamma(\mathbf{x})/2)$, where $c_0(\mathbf{x})$ is the velocity model defined at the reference frequency ω_0. The proportionality coefficients of two fractional Laplacians, separately stand for dispersion and absorption, are given by $\eta(\mathbf{x}) = -c_0^{2\gamma(\mathbf{x})}(\mathbf{x})\omega_0^{-2\gamma(\mathbf{x})}\cos(\pi\gamma(\mathbf{x}))$ and $\tau(\mathbf{x}) = -c_0^{2\gamma(\mathbf{x})-1}(\mathbf{x})\omega_0^{-2\gamma(\mathbf{x})}\sin(\pi\gamma(\mathbf{x}))$.

Equation 1 seems to be attractive for Q-RTM owing to its flexibility for separately compensating amplitude loss and correcting phase distortion. Treeby et al. (2010) and Zhu et al. (2014) state that attenuation compensation based on this equation can be achieved by reversing the absorption proportionality coefficient in sign but leaving the equivalent dispersion parameter unchanged. Zhu et al. (2014) implement Q-RTM applying the zero-lag cross-correlation imaging condition:

$$I(\mathbf{x}) = \int_0^T p_s(\mathbf{x},t)p_r(\mathbf{x},t)dt, \qquad (2)$$

where T denotes the maximal extrapolation time, the source wavefield $p_s(\mathbf{x},t)$ and receiver wavefield $p_r(\mathbf{x},t)$ are compensated

simultaneously. Q-compensated source wavefield $p_s(\mathbf{x}, t)$ is the solution of the following compensated equation:

$$\begin{cases} \frac{1}{c^2(\mathbf{x})}\frac{\partial^2 p_s}{\partial t^2}(\mathbf{x},t) - \eta(\mathbf{x})(-\nabla^2)^{\gamma(\mathbf{x})+1}p_s(\mathbf{x},t) + \tau(\mathbf{x})\frac{\partial}{\partial t}(-\nabla^2)^{\gamma(\mathbf{x})+1/2}p_s(\mathbf{x},t) = \delta(\mathbf{x}-\mathbf{x}_s)f(t), \\ p_s(\mathbf{x},t) = \frac{\partial p_s}{\partial t}(\mathbf{x},t) = 0, \mathbf{x}\in\Omega, t<0. \end{cases}$$

(3)

Similarly, Q-compensated receiver wavefield $p_r(\mathbf{x}, t)$ satisfies the following compensated equation:

$$\begin{cases} \frac{1}{c^2(\mathbf{x})}\frac{\partial^2 p_r}{\partial t^2}(\mathbf{x},t) - \eta(\mathbf{x})(-\nabla^2)^{\gamma(\mathbf{x})+1}p_r(\mathbf{x},t) + \tau(\mathbf{x})\frac{\partial}{\partial t}(-\nabla^2)^{\gamma(\mathbf{x})+1/2}p_r(\mathbf{x},t) = \delta(\mathbf{x}-\mathbf{x}_r)g(\mathbf{x},T-t), \\ g(\mathbf{x},t) = p(\mathbf{x},t), \quad \mathbf{x}\in\mathbf{x}_r, \quad t\in[0,T], \end{cases}$$

(4)

where $\mathbf{x}_r$ denotes the receiver positions and $g(\mathbf{x}, t)$ stands for the recorded data, which are reversed in time and enforced as the Dirichlet boundary condition at the receivers. However, amplitude compensation in equations 3 and 4 is a nonstationary process with energy exponentially amplified over the traveltime, which indeed boosts high-frequency ambient noise and even results in numerical instability. In the next section, we will develop a novel stabilization scheme for Q-RTM, thereby generating higher resolution and higher fidelity images.

Numerical simulation for the constant-Q wave equation with DFLs

As we can see from equation 1, the orders of fractional Laplacians are spatially varying, and they are difficult to incorporate into PSM. Zhu and Harris (2014) adopt the average value of the spatially varying orders for numerical simulation. The average scheme is only reasonable for smoothly heterogeneous Q models, but it is unsuitable for relatively sharp Q contrasts. Chen et al. (2016) develop two efficient fast Fourier transform (FFT)-based modeling schemes for constant-Q wave equation with DFLs. Both of these two schemes can efficiently cope with the spatial variable-order fractional Laplacians. In this paper, we use the first scheme proposed by Chen et al. (2016) to numerically simulate constant-Q wave equation with DFLs, which adopts the weighted sum of two constant-order fractional Laplacians to approximate the spatial variable-order fractional Laplacian.

First, we adopt the generalized Fourier PSM (Carcione, 2010) to define the wavenumber response of the fractional Laplacians, e.g.,

$$(-\nabla^2)^{\gamma(\mathbf{x})+1}p(\mathbf{x}, t) = \mathcal{F}^{-1}\{|\mathbf{k}|^{2\gamma(\mathbf{x})+2}\mathcal{F}[p](\mathbf{k}, t)\}, \quad (5)$$

where $\mathcal{F}$ and $\mathcal{F}^{-1}$ denote the forward and inverse Fourier transforms, respectively, and $|\mathbf{k}|$ is the norm of the complex wavenumber vector. Using the generalized Fourier PSM, we transform equation 1 into the wavenumber domain

$$\frac{1}{c^2(\mathbf{x})}\frac{\partial^2 p}{\partial t^2}(\mathbf{k},t) - \eta(\mathbf{x})|\mathbf{k}|^{2\gamma(\mathbf{x})+2}p(\mathbf{k},t) - \tau(\mathbf{x})\frac{\partial}{\partial t}|\mathbf{k}|^{2\gamma(\mathbf{x})+1}p(\mathbf{k},t)$$
$$= \delta(\mathbf{x}-\mathbf{x}_s)f(t).$$

(6)

Using the first approximation scheme proposed by Chen et al. (2016), we can rewrite the wavenumber responses of two fractional Laplacians in equation 6 as (refer to equation 9 in Chen et al., 2016)

$\eta(\mathbf{x})|\mathbf{k}|^{2\gamma(\mathbf{x})+2}$

$$\approx \lambda(\mathbf{x})\cos(\pi\gamma(\mathbf{x}))\left\{\left(1 - \frac{2\gamma(\mathbf{x})}{\varepsilon}\right)|\mathbf{k}|^2 + \frac{2\gamma(\mathbf{x})}{\varepsilon}\frac{1}{k_d^\varepsilon}|\mathbf{k}|^{2+\varepsilon}\right\}$$

(7)

and

$\tau(\mathbf{x})|\mathbf{k}|^{2\gamma(\mathbf{x})+1}$

$$\approx \lambda(\mathbf{x})\sin(\pi\gamma(\mathbf{x}))c_0^{-1}(\mathbf{x})\left\{\left(1 - \frac{2\gamma(\mathbf{x})}{\varepsilon}\right)|\mathbf{k}| + \frac{2\gamma(\mathbf{x})}{\varepsilon}\frac{1}{k_d^\varepsilon}|\mathbf{k}|^{1+\varepsilon}\right\},$$

(8)

where $\lambda(\mathbf{x}) = (\omega_d/\omega_0)^{\gamma(\mathbf{x})}$, $\omega_d = 2\pi f_d$ denotes the dominant angular frequency, f_d denotes the dominant frequency, and $k_d = \omega_d/c_0$ represents the dominant wavenumber. The parameter ε is introduced to guarantee $(|\mathbf{k}|/k_d)^\varepsilon$ sufficiently close to one; here, we choose $\varepsilon = 1/8$. From equations 7 and 8, we can find that spatially varying fractional Laplacians have been simplified into the weighted sum of two constant-order fractional Laplacians, which are easy to solve by PSM.

ADAPTIVE STABILIZATION FOR Q-RTM

Mathematically speaking, equations 3 and 4 are severely ill-posed due to the presence of the compensating term $+\tau\partial_t(-\nabla^2)^{\gamma+1/2}p(\mathbf{x}, t)$. To figure out exactly how the numerical instability arises and to lay a foundation for well-directed stabilization, we analytically derive k-space Green's functions for the constant-Q wave equation and its compensated equation. Because the form of Fourier kernel will affect the sign of temporal and spatial derivation (Holm and Nsholm, 2014), in this paper, we denote the space-time Fourier transform of a plane wave in a homogeneous attenuating medium as

$$\mathcal{F}[p](\mathbf{k}, \omega) = \int_{-\infty}^{\infty}\int_{\mathbb{R}^d}p(\mathbf{x},t)e^{-i(\omega t-\mathbf{kx})}d\mathbf{x}dt, \quad (9)$$

and the corresponding inverse Fourier transform as

$$\mathcal{F}^{-1}[p](\mathbf{x}, t) = \frac{1}{(2\pi)^d}\int_{-\infty}^{\infty}\int_{\mathbb{C}^d}p(\mathbf{k},\omega)e^{i(\omega t-\mathbf{kx})}d\mathbf{k}d\omega, \quad (10)$$

where $\mathbb{R}^d$ and $\mathbb{C}^d$ represent the d-dimensional real space and complex space, respectively, ω is the angular frequency, and $\mathbf{k}$ is the complex wavenumber vector.

The k-space Green's function

Assuming wave propagation in a homogeneous medium, we derive a k-space Green's function of equation 1 by enforcing a point source at time $t = t_0$ and at the location $\mathbf{x} = \mathbf{x}_s$. The time-space Green's function $G(\mathbf{x}, t)$ satisfies

$$\begin{cases} \frac{1}{c^2}\frac{\partial^2 G}{\partial t^2}(\mathbf{x},t) - \eta(-\nabla^2)^{\gamma+1}G(\mathbf{x},t) - \tau\frac{\partial}{\partial t}(-\nabla^2)^{\gamma+1/2}G(\mathbf{x},t) = -\delta(\mathbf{x}-\mathbf{x}_s)\delta(t-t_0), \\ G(\mathbf{x},t) = \frac{\partial G}{\partial t}(\mathbf{x},t) = 0, \quad \mathbf{x}\in\Omega, \quad t<t_0. \end{cases}$$

(11)

Application the space-time Fourier transform (as shown in equation 9) to equation 11 yields frequency-wavenumber harmonic

Green's function $G(\mathbf{k}, \omega)$, which is the solution of the following Helmholtz equation:

$$\left(\frac{\omega^2}{c^2} + \eta|\mathbf{k}|^{2\gamma+2} + i\omega\tau|\mathbf{k}|^{2\gamma+1}\right)G(\mathbf{k}, \omega) = \frac{1}{(2\pi)^{d+1}}e^{-i\omega t_0}e^{i\mathbf{k}\mathbf{x}_s}. \tag{12}$$

Solving for frequency-wavenumber harmonic Green's function $G(\mathbf{k}, \omega)$ and then applying $d+1$-dimensional inverse Fourier transform (as shown in equation 10), we have

$$G(\mathbf{x}, t) = \frac{c^2}{(2\pi)^{d+1}}\int_{-\infty}^{\infty}\int_{\mathbb{C}^d}h(\mathbf{k}, \omega)d\mathbf{k}d\omega, \tag{13}$$

where the integral kernel function is

$$h(\mathbf{k}, \omega) = \frac{e^{i\omega(t-t_0)}e^{-i\mathbf{k}(\mathbf{x}-\mathbf{x}_s)}}{\omega^2 + \eta|\mathbf{k}|^{2\gamma+2}c^2 + i\omega\tau|\mathbf{k}|^{2\gamma+1}c^2}. \tag{14}$$

The two singularities of this integral kernel function $h(\mathbf{k}, \omega)$ can be obtained by solving ω for the following equation:

$$\frac{\omega^2}{c^2} + \eta|\mathbf{k}|^{2\gamma+2} + i\omega\tau|\mathbf{k}|^{2\gamma+1} = 0. \tag{15}$$

This equation is also known as the dispersion relation of the decoupled constant-Q wave equation (Sun et al., 2014). The solutions of equation 15 are given by

$$\zeta_{1,2}(\mathbf{k}) = \pm\xi_1(\mathbf{k}) + i\xi_2(\mathbf{k}), \tag{16}$$

where $\xi_1(\mathbf{k}) = \sqrt{-\tau^2c^4|\mathbf{k}|^{4\gamma+2} - 4\eta c^2|\mathbf{k}|^{2\gamma+2}}/2$ and $\xi_2(\mathbf{k}) = -\tau c^2|\mathbf{k}|^{2\gamma+1}/2$ are the absolute real part and imaginary part of the solution, respectively. According to Cauchy's residue theorem, we deduce the analytical integration of $h(\mathbf{k}, \omega)$ with respect to ω (the detailed deduction is given in Appendix A),

$$\int_{-\infty}^{\infty}h(\mathbf{k}, \omega)d(\omega) = 2\pi\frac{\sin(\xi_1(\mathbf{k})t)e^{-\xi_2(\mathbf{k})t}}{\xi_1(\mathbf{k})}. \tag{17}$$

Therefore, this Green's function can be further expressed as

$$G(\mathbf{x}, t) = \frac{c^2}{(2\pi)^d}\int_{\mathbb{C}^d}\Gamma_{\text{att}}(\mathbf{k}, t)d\mathbf{k}, \tag{18}$$

where the attenuated time propagator $\Gamma_{\text{att}}(\mathbf{k}, t)$ is given by

$$\Gamma_{\text{att}}(\mathbf{k}, t) = \frac{\sin(\xi_1(\mathbf{k})t)e^{-\xi_2(\mathbf{k})t}}{\xi_1(\mathbf{k})}. \tag{19}$$

Similarly, Green's function for compensated equations 3 and 4 can be derived by reversing the absorption-related term τ in sign but leaving the other term η unchanged. We slightly modify Green's function $G(\mathbf{x}, t)$ to yield

$$G(\mathbf{x}, t) = \frac{c^2}{(2\pi)^d}\int_{\mathbb{C}^d}\Gamma_{\text{comp}}(\mathbf{k}, t)d\mathbf{k}, \tag{20}$$

where the compensated time propagator $\Gamma_{\text{comp}}(\mathbf{k}, t)$ is

$$\Gamma_{\text{comp}}(\mathbf{k}, t) = \frac{\sin(\xi_1(\mathbf{k})t)e^{\xi_2(\mathbf{k})t}}{\xi_1(\mathbf{k})}. \tag{21}$$

For lossless media, as $Q \to \infty, \gamma \to 0$, so $\eta \to -1$ and $\tau \to 0$, thus $\xi_1 = c_0|\mathbf{k}|, \xi_2 = 0$. The compensated time propagator $\Gamma_{\text{comp}}(\mathbf{k}, t)$ is identical to the attenuated time propagator $\Gamma_{\text{att}}(\mathbf{k}, t)$ in this situation. Here, we denote the acoustic time propagator as $\Gamma_{\text{aco}}(\mathbf{k}, t)$, and hence we have

$$\Gamma_{\text{aco}}(\mathbf{k}, t) = \Gamma_{\text{comp}}(\mathbf{k}, t) = \Gamma_{\text{att}}(\mathbf{k}, t) = \frac{\sin(c_0|\mathbf{k}|t)}{c_0|\mathbf{k}|}, \tag{22}$$

which further verifies that full acoustic/elastic medium can be considered as a time-invariant system. However, equations 19 and 21 further demonstrate that the time propagator of viscoacoustic-wave equation is no longer reversible due to the presence of the exponential terms $e^{-\xi_2(\mathbf{k})t}$ and $e^{\xi_2(\mathbf{k})t}$, where

$$\xi_2(\mathbf{k}) = \frac{1}{2}c_0^{2\gamma-1}\omega_0^{-2\gamma}\sin(\pi\gamma)c^2|\mathbf{k}|^{2\gamma+1} > 0, \quad \gamma \in \left(0, \frac{1}{2}\right). \tag{23}$$

According to equation 23, we can see clearly that the attenuated time propagator $\Gamma_{\text{att}}(\mathbf{k}, t)$ is convergent over the propagation time, whereas the compensated time propagator $\Gamma_{\text{comp}}(\mathbf{k}, t)$ is divergent at the high-wavenumber end, which results in numerical instability during compensation. That is to say, attenuating media can be considered as a time-variant system with seismic wave energy exponentially decreasing, contrarily, attenuation compensation is a nonstationary process with energy exponentially amplified over the propagation time. Furthermore, the exponentially decreased or increased speed is closely linked to the magnitude of wavenumber $|\mathbf{k}|$, which suggests that the high-wavenumber components are more vulnerable to be absorbed or amplified.

For a more intuitive understanding about the k-space Green's functions for constant-Q wave equation and its compensated equation, we further display the graphical representation of the attenuated and compensated time propagators. Here, we consider a 2D homogeneous model with $Q = 50$. Figure 1 displays the acoustic time propagator, attenuated time propagator, and compensated time propagator with the maximum traveltime of 1.0 s, respectively. Compared with the acoustic time propagator, the attenuated time propagator in Figure 1b exhibits weaker amplitude at a longer time, especially for high-wavenumber components; on the contrary, the compensated time propagator seems to be boosted at the high-wavenumber end, as shown in Figure 1c. To have a clear observation about the numerical instability resulting from such an exponentially amplified propagator, we further draw the compensated time propagator with a longer traveltime of 2.0 s. As shown in Figure 1d, high-wavenumber oscillations become increasingly intense over time, which eventually leads to numerical instability. Wang (2009) points out that the ambient noise generally comes from high-frequency noise in seismic data and the machine errors relative to working precision. Such an exponential propagator certainly boosts the ambient noise. Thus, stabilization in the spatial frequency domain is indispensable for eliminating the high-frequency oscillations.

In the following section, we will propose a novel stabilization scheme for *Q*-RTM.

Adaptive stabilization based on the k-space Green's function

Wang (2006) proposes a stabilized inverse-*Q* filtering for seismic resolution enhancement by using an amplitude-compensated operator with stabilization. Stabilized amplitude-compensated operator in the inverse problem can be expressed as (Wang, 2002; Irving and Knight, 2003; Berkhout, 2012)

$$\Lambda(\tau, \omega) = \frac{\beta(\tau, \omega)}{\beta^2(\tau, \omega) + \sigma^2}, \tag{24}$$

where $\beta(\tau, \omega)$ is an amplitude-attenuated operator and σ^2 is the stabilization factor. The stabilization exhibits inherent adaptability, compared with conventional low-pass filtering, by adaptively limiting the compensation of a given high-frequency wave component, which has been attenuated to a level below the ambient noise. In this paper, we propose a similar adaptive stabilization for *Q*-RTM. According to equations 21 and 23, we define the amplitude-attenuated operator $\beta(\mathbf{k}, t)$ as

$$\beta(\mathbf{k}, t) = e^{-\xi_2(\mathbf{k})t} = e^{-\frac{1}{2}c_0^{2\gamma-1}\omega_0^{-2\gamma}\sin(\pi\gamma)c^2|\mathbf{k}|^{2\gamma+1}t} \tag{25}$$

and the amplitude-compensated operator as

$$\Lambda(\mathbf{k}, t) = \beta^{-1}(\mathbf{k}, t) = e^{\xi_2(\mathbf{k})t}. \tag{26}$$

However, such an exponential compensation operator suffers from numerical instability. Then, the amplitude-compensated operator with adaptive stabilization can be defined as

$$\Lambda(\mathbf{k}, t) = \frac{\beta(\mathbf{k}, t)}{\beta^2(\mathbf{k}, t) + \sigma^2} = \frac{e^{\xi_2(\mathbf{k})t}}{1 + \sigma^2 e^{2\xi_2(\mathbf{k})t}}. \tag{27}$$

In fact, the compensation operator $e^{\xi_2(\mathbf{k})t}$ has been embodied in equations 3 and 4 by reversing the absorption proportionality coefficient in sign; therefore, we merely need to modify the *Q*-RTM scheme by introducing a stabilization operator given as

$$S(\mathbf{k}, t) = \frac{1}{1 + \sigma^2 e^{2\xi_2(\mathbf{k})t}}. \tag{28}$$

Wang and Guo (2004) propose a stabilized approach for inverse-*Q* filtered migration, and point out that one must evaluate the earth attenuation effect accumulated from the recording surface down to the current depth, not just the effect within the current extrapolation step. Accordingly, the attenuation and compensation effects in *Q*-RTM are considered to be accumulated from the starting time to the current time, and thus we need to perform stabilization at every time step Δt. Now, we define a stabilization coefficient $s(\mathbf{k}, l\Delta t)$ as

$$\prod_{l=1}^{n} s(\mathbf{k}, l\Delta t) = S(\mathbf{k}, n\Delta t). \tag{29}$$

This coefficient is considered as a supersedent to the exponentially divergent time propagator, and it will be used for *Q*-RTM within the *l*th time-step extrapolation. For the first step $l = 1$, the stabilization coefficient is

$$s(\mathbf{k}, \Delta t) = S(\mathbf{k}, \Delta t) = \frac{1}{1 + \sigma^2 e^{2\xi_2(\mathbf{k})\Delta t}}, \tag{30}$$

and for the *l*th time step, it is given by

$$s(\mathbf{k}, l\Delta t) = \frac{S(\mathbf{k}, l\Delta t)}{S(\mathbf{k}, (l-1)\Delta t)} = \frac{1 + \sigma^2 e^{2\xi_2(\mathbf{k})(l-1)\Delta t}}{1 + \sigma^2 e^{2\xi_2(\mathbf{k})l\Delta t}},$$
$$l = 2, 3, \ldots, n. \tag{31}$$

To illustrate inherent adaptability of such a stabilization scheme, we numerically compare the spatial frequency-dependent compensation curves $\Lambda(\mathbf{k}, t)$ at different traveltime t and with different quality factor *Q*. We assume that reference velocity of the homogeneous medium is 3000 m/s at a specific angular frequency $\omega_0 = 20\pi f_d$ (Carcione, 2008; Sun et al., 2014), where $f_d = 30$ Hz denotes the dominant frequency of the Ricker wavelet. Figure 2a shows three gain curves at $t = 0.5, 1.0$, and 1.5 s, respectively, with $Q = 30$ and $\sigma^2 = 0.1\%$. These curves have the same peak amplitude value but various frequency band range, more specifically, the effective compensation range shifts to low frequency and becomes more and more narrow over time. As shown in Figure 2b, similarly, *Q*-values also influence the spatial frequency distribution of the compensation curves, which moves toward low frequency as the
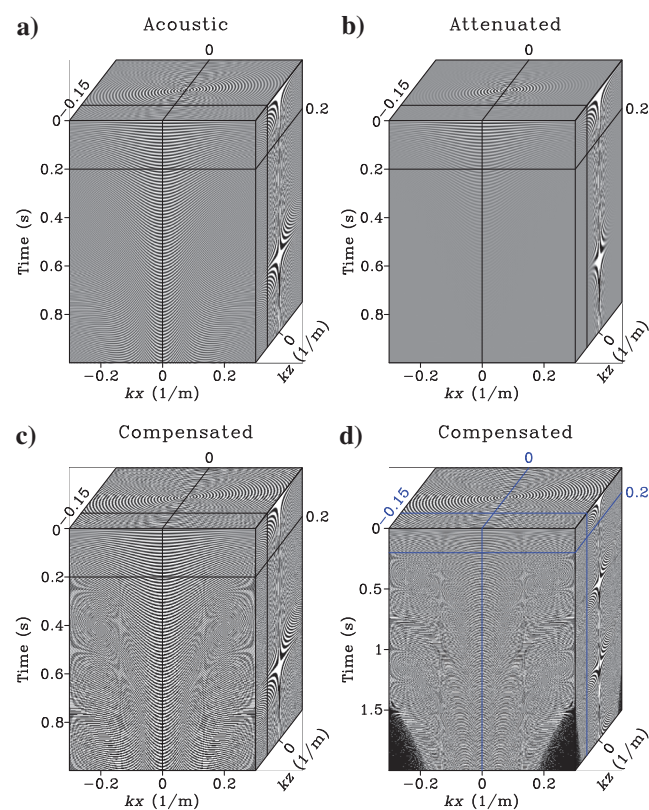

Figure 1. Time propagators of *k*-space Green's functions for: (a) acoustic-wave equation, (b) constant-*Q* wave equation, (c) compensated constant-*Q* wave equation with maximum traveltime of 1.0 s, and (d) compensated constant-*Q* wave equation with maximum traveltime of 2.0 s. We clip the same amplitude value for all four figures. Note that high-wavenumber instability can be observed from panel (d).

Q-value decreases ($Q = 120$, 60, and 30). In general, the rules of stabilized compensation curves varying with traveltime t and quality factor Q tally with our intuitive understanding. Considering seismic wave propagation in high-attenuation media with smaller Q, when it travels a longer time, its amplitude undergoes more intensive attenuation, especially for high-frequency components; accordingly, Q-compensation trends to drastically amplify such attenuated signal even ambient noise, whereas amplitude-compensated operator with stabilization can adaptively avoid boosting the ambient noise by high-frequency suppression. Thus, it indicates that this stabilized compensation is a nonstationary and adaptive process.

Adaptive stabilization versus low-pass filtering

Typically, numerical instability resulting from boosted high-frequency noise can be modestly relieved by low-pass filtering in the frequency domain (Wang, 2009) or in the wavenumber domain (Treeby et al., 2010; Zhu et al., 2014). Wang (2009) points out that a desirable low-pass filter should be time variant and Q dependent. However, it is impractical to design such an adaptive filter. In fact, this intelligent property is naturally built into our proposed stabilization scheme. As we have seen, the amplitude-compensated operator with stabilization can adaptively vary with traveltime t and quality factor Q; thus, it can avoid boosting ambient noise. What we should pay attention to is that the stabilization factor σ^2 as a customized parameter greatly influences the fidelity and stability of compensation. Furthermore, this factor is physically linked to the signal-to-noise ratio (S/N) of the seismic data. In this section, we will formulate an empirical algorithm for identifying the stabilization factor and then compare it with conventional low-pass filtering.

Wang (2006) proposes an empirical formula for estimating the stabilization factor σ^2 from a specific gain limit $G_{\lim}$, where $G_{\lim}$ corresponds to maximal amplitude gain in decibels, i.e.,

$$G_{\lim} := 20 \log_{10}\left\{\max_{\forall \mathbf{k} \in \mathbb{C}^d, \forall t > 0} S(\mathbf{k}, t)\right\}. \tag{32}$$

Similarly, we can formulate an explicit relationship between the stabilization factor σ^2 and user-specified gain limit $G_{\lim}$ by linear fitting. As shown in Figure 3a, where $Q = 30$ and $t = 1.5$ s are assumed, the stabilized amplitude-compensated operators with a series of stabilization factors σ^2 (from 10% to 0.0001%) have distinct compensation ranges. This observation suggests that the stabilization factor σ^2 directly determines the balance between the fidelity and stability of compensation. The smaller is the stabilization factor σ^2, the more broadly it will compensate. Then, we plot the peak of each gain curve in decibels (Figure 3b), it shows that the gain limit can be given as

$$G_{\lim} = -4.343 \ln \sigma^2 - 6.021. \tag{33}$$

Thus, we can identify the stabilization factor σ^2 from a specific gain limit $G_{\lim}$ by following an empirical formula:

$$\sigma^2 = e^{-0.23G_{\lim} - 1.39}. \tag{34}$$

Stabilization by low-pass filtering is equivalent to applying a high-cut filter to the nonstabilized compensation operator, it can be symbolically represented as
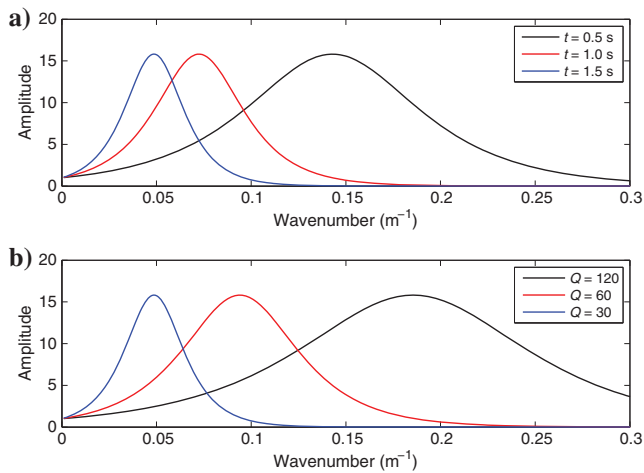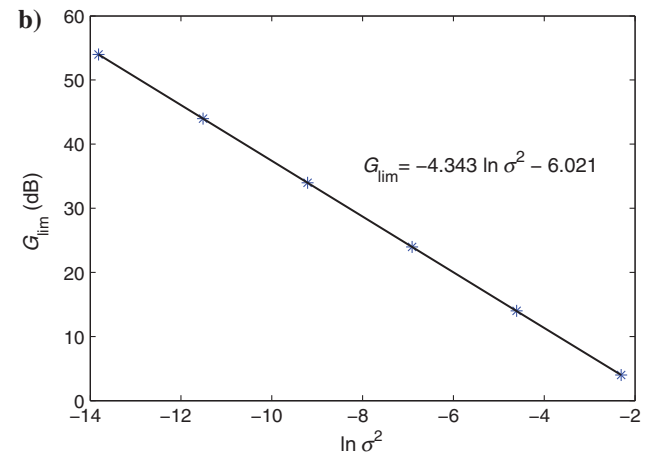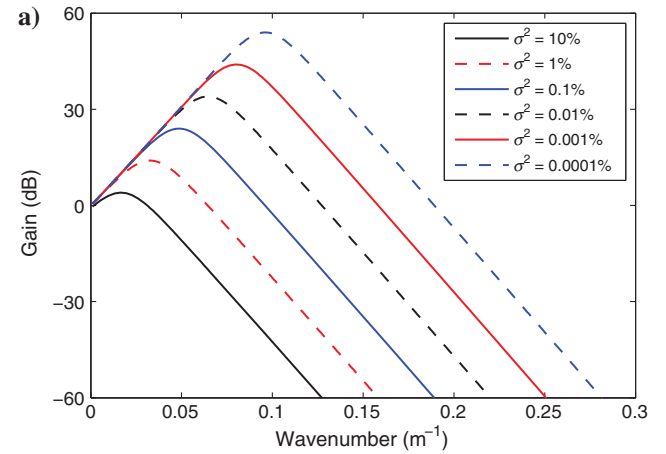

Figure 2. The stabilized compensation coefficients $\Lambda(\mathbf{k}, t)$ varying with (a) different traveltimes $t = 0.5$, 1.0, and 1.5 s ($Q = 30$ and $\sigma^2 = 0.1\%$), and (b) different quality factors $Q = 120$, 60, and 30 ($t = 1.5$ and $\sigma^2 = 0.1\%$).

Figure 3. (a) The stabilized compensation curves $\Lambda(\mathbf{k}, t)$ (in decibels) varying with a series of stabilization factors σ^2 (from 10% to 0.0001%), and (b) linear fitting for gain limit $G_{\lim}$ varying with $\ln \sigma^2$.

$$\Pi(\mathbf{k}, t) = \mathcal{A}[\Lambda](\mathbf{k}, t) = \Lambda_{|\mathbf{k}| \le \rho}(\mathbf{k}, t), \qquad (35)$$

where $\mathcal{A}$ is a low-pass filtering operator and parameter ρ denotes the cut-off spatial frequency of the filter. Here, we choose a Tukey window for suppressing the amplification of high-frequency noise during attenuation compensation. The cut-off wavenumber of the low-pass filter is usually identified by estimating the noise level from the power spectrum of the measured data (Zhu et al., 2014). Thus, the cursory truncation results in the filter to be time invariant and Q independent. The Tukey windows with different taper ratios α and cut-off parameters ρ are shown in Figure 4a, and their spectrum responses are shown in Figure 4b. As we can see from Figure 4b, the more sharply the window edge changes, the more intensely the side lobe of spectrum oscillates. It means that sharply truncating the high-frequency components of the compensated data may result in the Gibbs ringing artifacts, which manifests itself as spurious ringing around sharp edges (Ammari, 2008; Sun and Zhu, 2015). A feasible approach to reduce the Gibbs ringing artifact is to filter the compensated wavefield by a smoothed window.

For a fair comparison between the compensation curves $\Lambda(\mathbf{k}, t)$ regularized by adaptive stabilization and the compensation curves $\Pi(\mathbf{k}, t)$ trapped by Tukey windows, we consider the Pierre Shale model that exhibits homogeneous attenuating property with $Q = 30$, and the noise level of the measured data is -60 dB. We set the gain limit $G_{\lim} = 40$ dB for stabilization, which corresponds to stabilization factor $\sigma^2 = 0.0025\%$. Figure 5 displays gain curves using two kinds of stabilized compensation schemes at different traveltimes $t = 0.5, 1.0,$ and 1.5 s. Figure 5a shows that the peak gains of compensation curves with stabilization are not affected by traveltime, which maintains a fixed gain limit $G_{\lim}$ of 40 dB. As we have claimed in the previous section that the effective compensation range of $\Lambda(\mathbf{k}, t)$ shifts to low-frequency end over time. Figure 5b displays the compensation operators $\Pi(\mathbf{k}, t)$ trapped by Tukey windows with the cut-off wavenumber $\rho = 0.14$ m^{-1}. The cut-off parameter is chosen for maintaining the gain limit $G_{\lim} \le 40$ dB within 1.0 s, and it corresponds to the cut-off frequency of 80 Hz. Unlike the gain curve regularized by our proposed stabilization scheme, the gain curve trapped by low-pass filter has different gain limit $G_{\lim}$ but maintains a fixed passband. It indicates that our proposed adaptive stabilization can be considered as a time-varying filter.

As is shown in Figure 1d, the high-wavenumber oscillatory becomes increasingly intense over time, which eventually leads to numerical instability. Here, we apply the aforementioned stabilization methods into compensated time propagator, Figure 6 shows the compensated time propagators stabilized by low-pass filtering and our proposed scheme, respectively. We set $\sigma^2 = 2.5 \times 10^{-7}$ for our proposed method, and cut-off wavenumber $\rho = 0.16$ m^{-1} for the high-cut filter. From Figure 6a and 6b, we can conclude that our proposed stabilization scheme preserves more high-wavenumber components at a short propagation time, and it prevents the propagator from being unstable by suppressing the high-wavenumber components at a larger time; whereas low-pass filtering may result in a high-wavenumber loss in a short period of time and a relatively high-wavenumber divergence over a long period of time.

To further verify our conclusion, we compare wavenumber traces extracted from the compensated time propagators in Figure 6 with fixed $k_z = 0.2$ m^{-1} at $t = 0.5, 1.0,$ and 1.5 s, respectively. As shown

in Figure 7, the trace of the compensated time propagator stabilized by our proposed method (the red line) can well match with the compensated trace (black line) within the full-wavenumber band at a short
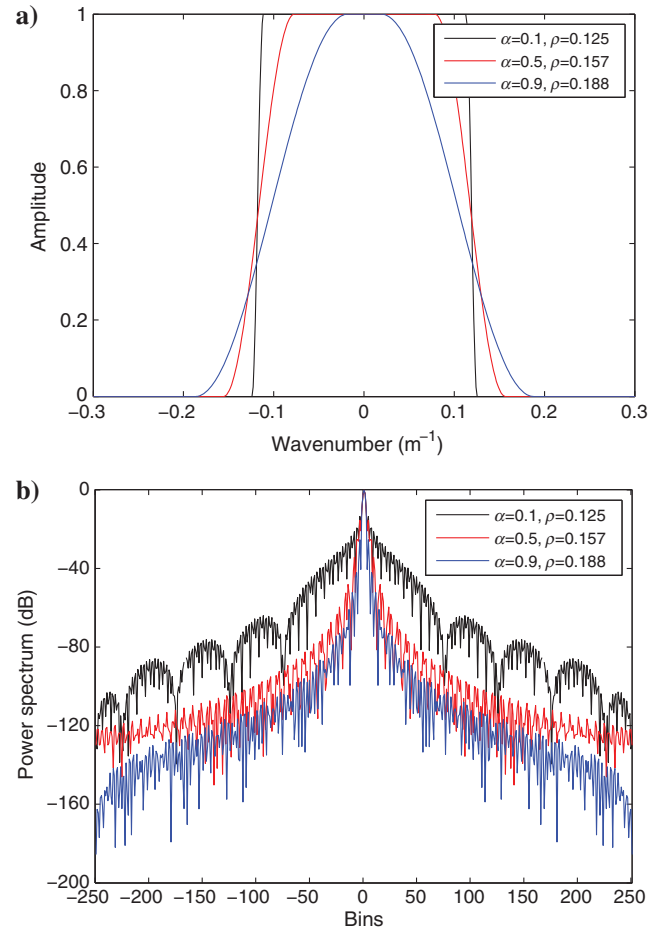

Figure 4. Tukey windows and their power spectra with different taper ratios α and cut-off parameters ρ: (a) Tukey windows and (b) their power spectra.
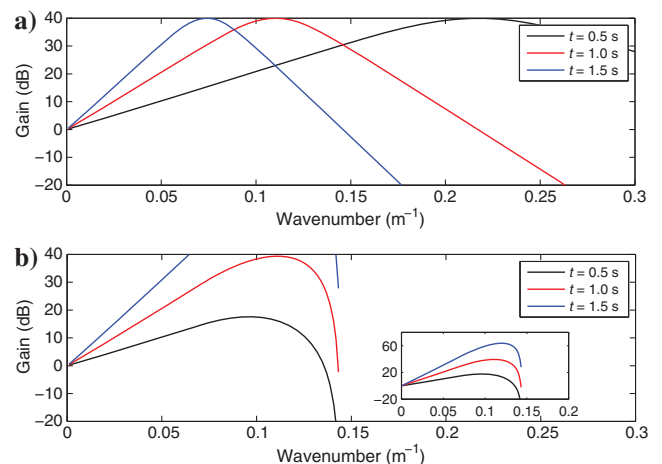

Figure 5. The compensation curves (in decibels) at different traveltimes $t = 0.5, 1.0,$ and 1.5 s, which is stabilized by (a) adaptive stabilization ($\sigma^2 = 0.0025\%$) and (b) low-pass Tukey filtering ($\rho = 0.14$ m^{-1}).
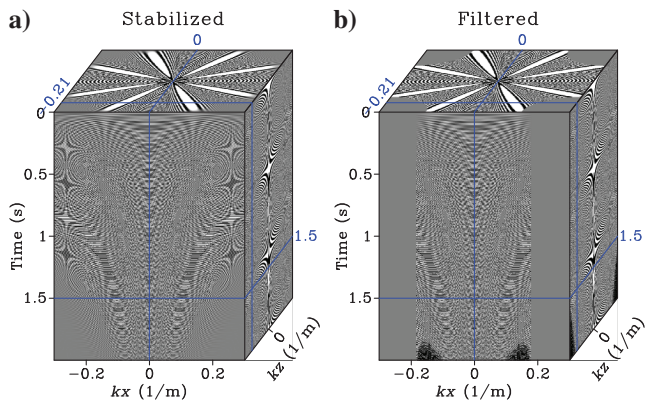
a) Stabilized   **b)** Filtered

Figure 6. The compensated time propagators stabilized by (a) adaptive stabilization ($\sigma^2 = 2.5 \times 10^{-7}$) and (b) low-pass Tukey filtering ($\rho = 0.16$ m^{-1}). We clip the same amplitude value for these two figures.
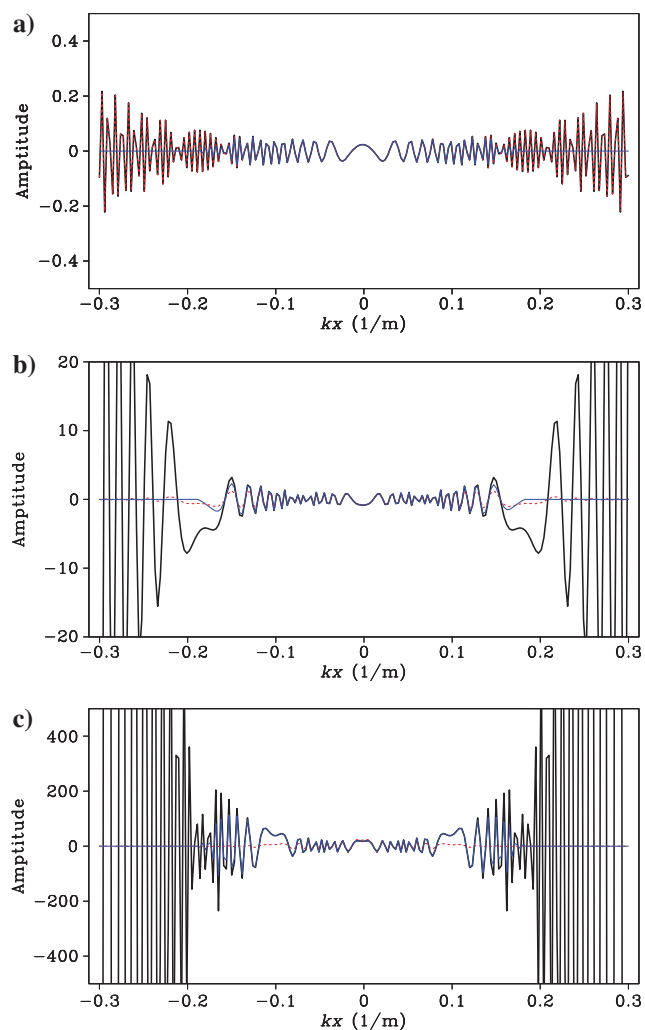
propagation time (Figure 7a), whereas that of the low-pass filtered propagator (the blue line) suffers from high-wavenumber loss. After a relatively long traveltime, the compensated time propagator tends to be boosted at the high-wavenumber end. In such a situation, our stabilization scheme still maintains a stable propagator; however, it is not the case for low-pass filtering. Furthermore, Figure 8 compares several time traces extracted from the compensated time propagators in Figure 6 at low, medium, and high wavenumbers, respectively, from which we can draw a similar conclusion.

In brief, we can make two observations from Figures 6–8. First, both of these two stabilized methods mostly overcome the numerical instability by recovering low- and medium-frequency seismic signal and suppressing the high-frequency artifact. Second, compensation with adaptive stabilization exhibits superior property of time variance and Q dependence, as the stabilized gain curve is automatically adjusted with traveltime t and quality factor Q. Therefore, it can intelligently avoid boosting the ambient noise,

Figure 7. Wavenumber traces extracted from compensated time propagators in Figure 6 with fixed $k_z = 0.2$ m^{-1} at: (a) $t = 0.5$, (b) 1.0, and (c) 1.5 s, where the solid black line corresponds to compensated trace without stabilization, the red line corresponds to adaptively stabilized trace, and the blue line corresponds to low-pass filtered trace.
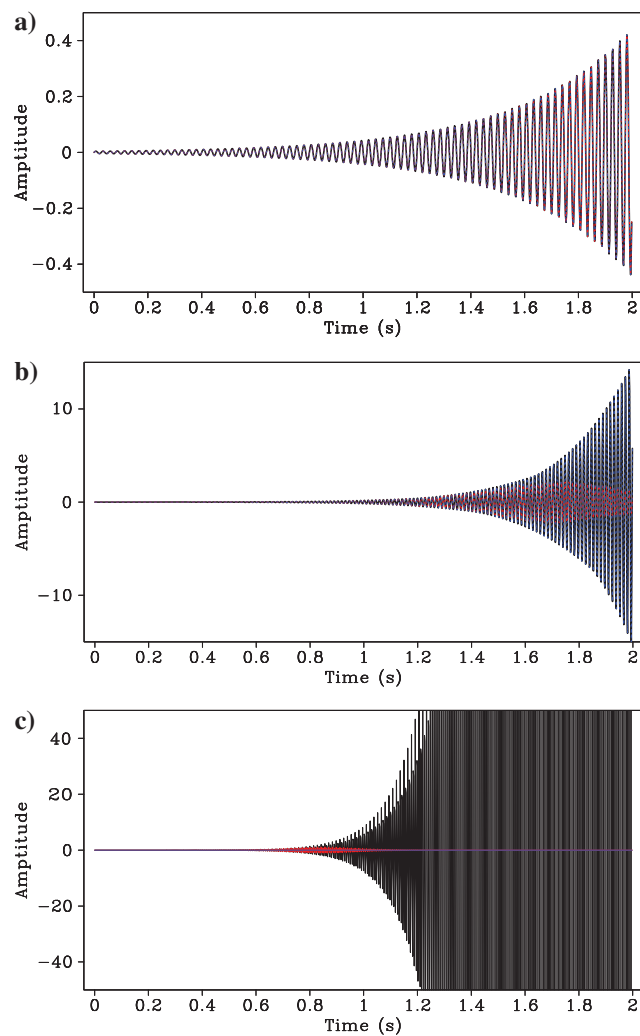
Figure 8. Time traces extracted from compensated time propagators in Figure 6 at low, medium, and high wavenumbers: (a) $\rho = 0.05$, (b) 0.15, and (c) 0.20 m^{-1}, where the solid black line corresponds to a compensated trace without stabilization, the red line corresponds to an adaptively stabilized trace, and the blue line corresponds to a low-pass filtered trace.

especially for the noisy data. More specifically, in a short period of propagation time, both methods can recover low- and medium-wavenumber components; nevertheless, our adaptive stabilization tends to compensate more high-frequency components than conventional low-pass filtering method. In a long period of propagation time, the compensation range of both methods move toward low wavenumber, compensation with stabilization can better suppress medium-frequency components. In the next section, we will demonstrate the superiority of adaptive stabilization over low-pass filtering in terms of *Q*-RTM quality.

Q-RTM EXAMPLES OF SYNTHETIC DATA

As we have seen in the previous section, *Q*-RTM using our proposed adaptive stabilization scheme can theoretically recover as many high-frequency components of shallow structures as possible, and at the same time maintain relatively stable compensation for deep structures. To numerically demonstrate the superiority of adaptive stabilization over conventional low-pass filtering, we perform *Q*-RTM on two synthetic models with the high-attenuation gas-bearing area, respectively, stabilized by low-pass filtering and our proposed method. Conventional RTM for such attenuating model may cause insufficient illumination under the gas-bearing area. Furthermore, *Q*-RTM with noisy data is also considered for verifying the antinoise performance of our proposed stabilization scheme.

Simple five-layer model

We consider *Q*-RTM for a simple five-layer model, whose velocity and *Q* models are, respectively, shown in Figure 9a and 9b. A high-attenuation gas-bearing wedge is located at the third layer

of the model. The size of the model is 2×3 km with a grid spacing of $dx = dz = 10$ m. There are 61 shots distributed laterally with the shot interval $ds = 50$ m; each of them is accompanied with 201 double-sided receivers. The source function is a Ricker wavelet with a dominant frequency of $f_d = 20$ Hz. To identify a reasonable cut-off frequency for conventional filtered *Q*-RTM and stabilization factor for our proposed stabilized *Q*-RTM, we need to estimate the noise level of the measured data (Zhu et al., 2014). Figure 10 shows synthetic shot gathers in an acoustic medium (Figure 9a) and in a viscoacoustic medium (Figure 9b), respectively, we can observe apparent amplitude decay in the viscoacoustic gather. Figure 11a displays traces selected arbitrarily at the distance of 1000 m from shot gathers in Figure 10; there is a slight phase dislocation between these two traces. Their power spectra are shown in Figure 11b, from

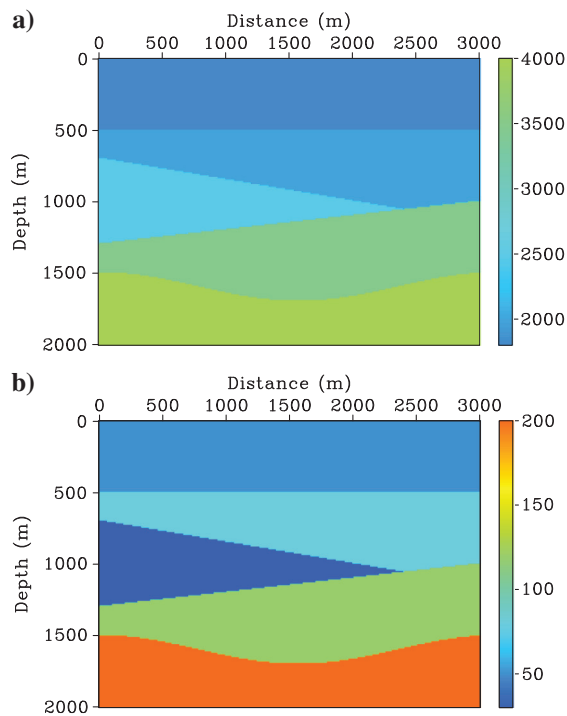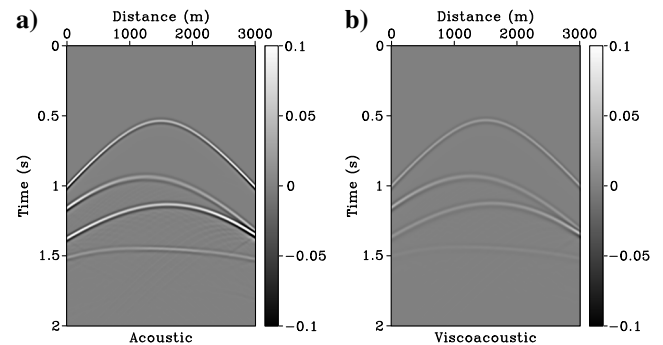Figure 10. Synthetic shot gathers in the (a) acoustic and (b) viscoacoustic media shown in Figure 9.

Figure 9. (a) Velocity model and (b) *Q* model of a simple five-layer model, which contains a high-attenuation gas-bearing wedge exhibiting an extreme attenuating property with $Q = 30$.
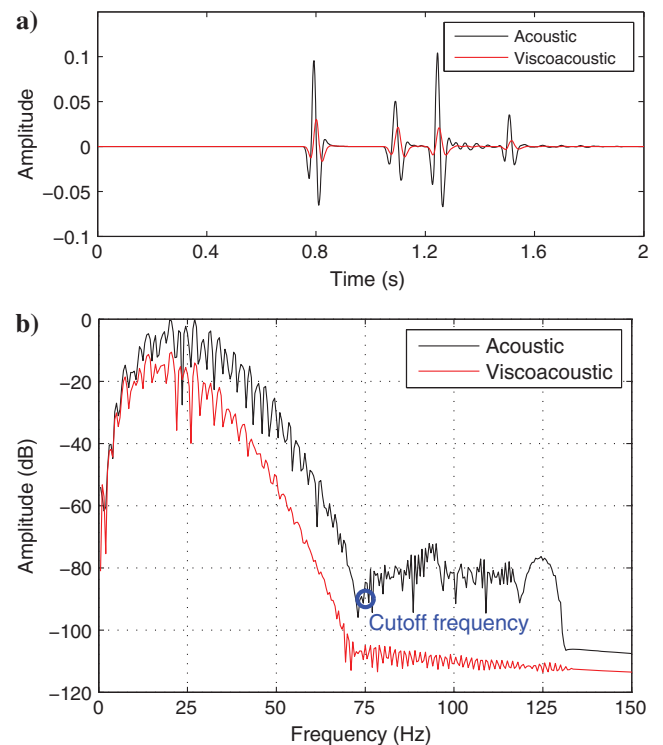

Figure 11. (a) Synthetic traces selected arbitrarily at a distance of 1000 m from shot gathers in Figure 10 and (b) their power spectra.

which we select a cut-off frequency of 75 Hz for the Tukey filter (the blue circle marked in Figure 11b). Remarkably, the cut-off frequency f_c is calculated by multiplying the cut-off wavenumber k_c by the maximum velocity c_{max} of the simulated model (Zhu et al., 2014). Accordingly, we adopt a gain limit G_{lim} of 60 dB for our proposed stabilized Q-RTM to maintain stable compensation, which corresponds to a stabilization factor $\sigma^2 = 2.5 \times 10^{-7}$.

Figure 12a shows the migrated image as a reference using conventional RTM from acoustic data; the imaging result of RTM (Figure 12b) from viscoacoustic media without compensation exhibits reduced amplitude and distorted phase compared with the reference. The compensated images of Q-RTM stabilized by low-pass filtering and the proposed scheme are shown in Figure 12c and 12d, respectively. From these migrated images, we can reach two conclusions. First, compared with the noncompensated image in Figure 12b, the compensated images (Figure 12c and 12d), no matter obtained by the filtered Q-RTM or stabilized Q-RTM, have a clear improvement. Second, because Q-RTM with adaptive stabilization exhibits the superior properties of time variance and Q dependence, it can recover as many high-frequency components of shallow structures as possible, and at the same time prevent the ambient noise from being boosted. A more intuitive comparison is made by extracting single traces from these migrated images. Figure 13 shows the vertical, horizontal, and sloping profile extracted from the images in Figure 12. As shown in Figure 13a, the trace extracted from the noncompensated image obtained from viscoacoustic data using conventional RTM suffers from amplitude attenuation and phase distortion compared with that from the nonattenuated image. Another two profiles shown in Figure 13b and 13c are picked along the first horizontal reflection and the third incline reflection, where the compensated trace using our proposed stabilization scheme matches the reference trace better owing to its property of amplitude preserving and intelligent adjustment of the compensation band, especially for shallow reflections.

BP gas chimney model

To further demonstrate the stability and reliability of our proposed stabilization scheme, we conduct Q-RTM on the BP gas chimney model with clean data and noisy data, respectively. Figure 14a and 14b shows its velocity and Q models (Zhu et al., 2014), which contains a high-attenuation gas chimney exhibiting an extreme attenuating property with $Q = 20$. The model has 161 nodes with a sampling interval of $dz = 10$ m in depth and 398 nodes with sampling interval of $dx = 10$ m in the horizontal direction. In the observation system, 80 sources are distributed laterally with a shot interval $ds = 50$ m, and each shot has 161 double-sided receivers with a maximum offset of 0.8 km. The point source is a Ricker wavelet with a dominant frequency $f_d = 30$ Hz. The synthetic seismic data are modeled by the PSM with time interval $dt = 0.001$ s, and the records last 2 s.

Q-RTM with clean data

In this example, we first consider Q-RTM for BP gas chimney model without any noise. In such an ideal situation, attenuation compensation is still prone to generate high-frequency artifacts and even to result in numerical instability because the ambient noise coming from the machine errors relative to working precision will be exponentially boosted (Wang, 2009). Therefore, reasonable stabilization needs to be incorporated to obtain a higher resolution and higher fidelity image. In this example, we conduct Q-RTM using two different stabilization schemes: conventional low-pass filtering with the cut-off frequency of 80 Hz (Zhu et al., 2014), and adaptive stabilization with gain limit $G_{lim} = 40$ dB (corresponding to $\sigma^2 = 0.0025\%$).

Figure 15 shows several migrated images obtained using acoustic RTM, viscoacoustic RTM without compensation, low-pass-filtered Q-RTM, and adaptively stabilized Q-RTM, respectively. For these, the acoustic imaging result shown in Figure 15a serves as a reference for comparison. Due to the presence of a high-attenuation gas chimney, the imaging result of gas trap shown in the blue frame in Figure 15b exhibits attenuated amplitudes and blurred structures; besides, the extreme attenuating area also gravely affects the migration image of the anticlinal structure below the gas trap, and the bulge located over the left wing of the anticline shown in the green frame in Figure 15b is almost invisible. Figure 15c and 15d shows compensated images using Q-RTM stabilized by low-pass filtering and our proposed scheme, respectively. Both of these two compensated images exhibit clear anticlinal structure and recovered amplitudes, whereas the image in Figure 15d presents better amplitude-preserving performance compared to the image in Figure 15c.

Figure 16 compares migrated seismic traces that are selected arbitrarily at three distances of 1500, 2200, and 3200 m from the imaging results shown in Figure 15. The blue frames on these traces display the contrast of shallow structures, whereas the green frames highlighting deep structures are shown with a gain of 10. The first trace is the reference migration result without attenuation (Figure 15a). Trace 2 stands
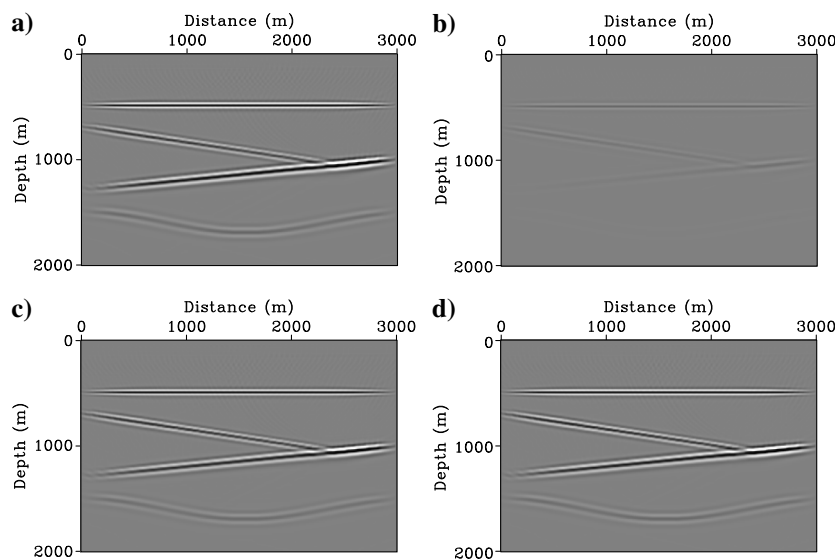

Figure 12. Migrated images of the simple five-layer model using (a) conventional RTM from acoustic data, (b) conventional RTM from viscoacoustic media without compensation, (c) low-pass-filtered Q-RTM, and (d) adaptively stabilized Q-RTM.

for the result of the noncompensated image (Figure 15b). Trace 3 is selected from the image generated by low-pass-filtered *Q*-RTM (Figure 15c), whose deep structures are still blurred because of the limited compensation depth and frequency bands. The last trace is the *Q*-RTM image regularized by our proposed stabilization scheme (Figure 15d), which is comparable with the ideal situation of pure acoustic media (trace 1). Figure 17 shows their amplitude spectra, from which we can conclude that *Q*-RTM with adaptive stabilization tends to recover the amplitude of reflected waves in a broader frequency band compared with *Q*-RTM using low-pass filtering. From Figure 17a–17c, we can note that the high-wave-number components of seismic traces crossing the high-attenuation gas chimney are not fully recovered by filtered *Q*-RTM or stabilized *Q*-RTM. This phenomenon is consistent with our intuition that seismic waves traveling through the high-attenuation gas chimney undergo severer attenuation; thus, the attenuated high-wavenumber components may suffer from more severe suppression during compensation.

Q-RTM with noisy data

To facilitate the comparison between low-pass filtering and our proposed stabilization scheme in terms of antinoise performance and resolution enhancement, we further consider *Q*-RTM for noisy data, in which we add 5% band-pass-filtered random noise to the seismic records (Wang, 2006). Figure 18a shows synthesized records from the BP gas chimney model, and Figure 18b shows the noisy data, which consist of the synthetic data and 5% band-pass-filtered random noise. Because high-frequency random noise
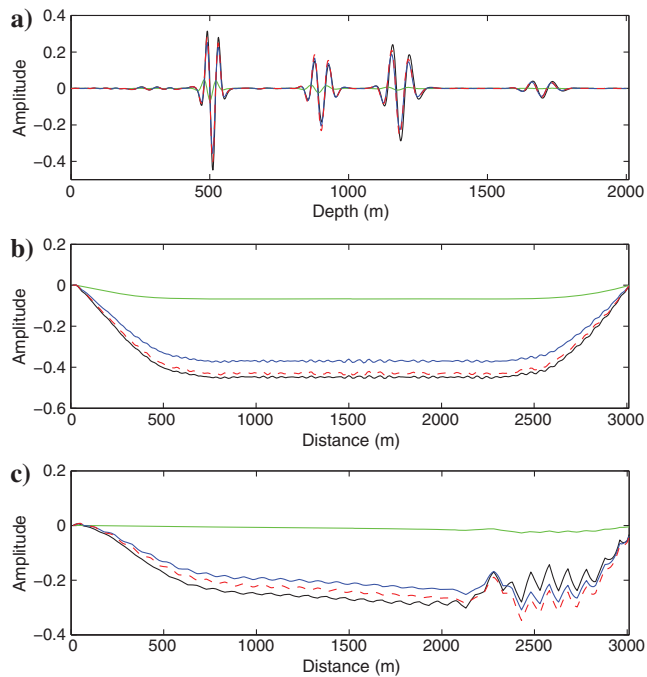

Figure 13. Profiles extracted from the images in Figure 12: (a) vertical profile at $X = 1500$ m, (b) horizontal profile at $Z = 500$ m, and (c) sloping profile along the third horizon. The solid black line corresponds to reference image, the green line corresponds to the image without compensation, the blue line corresponds to the low-pass filtered *Q*-RTM image, and the dashed red line corresponds to the adaptively stabilized *Q*-RTM image.

is more vulnerable to being boosted during compensation, a lower cut-off frequency for the Tukey filter and a lower gain limit G_{lim} (or bigger stabilization factor σ^2) for stabilization should be selected to overcome the numerical instability. Figure 19a shows a noise-free trace and a noisy trace selected from shot 40 shown in Figure 18, and Figure 19b shows their amplitude spectra. As shown in Figure 19b, the effective compensation band of the clean trace is within 75 Hz indicated by the blue circle, whereas that of the noisy trace is within 140 Hz; thus, high-frequency components within 75–140 Hz will be boosted during attenuation compensation. In this example, three different cut-off frequencies $\rho = 60$, 75, and 90 Hz are chosen for filtered *Q*-RTM, and stabilization factors $\sigma^2 = 0.25\%$, 0.025% and 0.0025% (corresponding to $G_{\text{lim}} = 20$, 30, and 40 dB, respectively) are adopted for our stabilized *Q*-RTM.

Figure 20a, 20c, and 20e shows the compensated migration images obtained by filtered *Q*-RTM corresponding to $\rho = 60$, 75, and 90 Hz, respectively, and Figure 20b, 20d, and 20f displays those obtained by stabilized *Q*-RTM corresponding to $\sigma^2 = 0.25\%$, 0.025%, and 0.0025%. As we can see from Figure 20a, 20c, and 20e, the anticline under the high-attenuation gas chimney becomes increasingly clearer with the increase of the cut-off frequency in filtered *Q*-RTM, whereas the image of the gas chimney is flooded by boosted medium- and high-frequency noise. A relatively low cut-off frequency is therefore chosen to improve the imaging quality of the gas trap at the expense of the under-compensated deep structures. As seen from Figure 20b, 20d, and 20f, the fidelity of the deep structures is improved as the stabilization factors decrease; nevertheless, excessively reducing the stabilization factor results in numerical instability during compensation. On the whole, the compensation performance of *Q*-RTM for noisy data degrades slightly against the noise-free case (Figure 15), adaptive stabilized *Q*-RTM exhibits better antinoise performance and amplitude fidelity than low-pass-filtered *Q*-RTM.
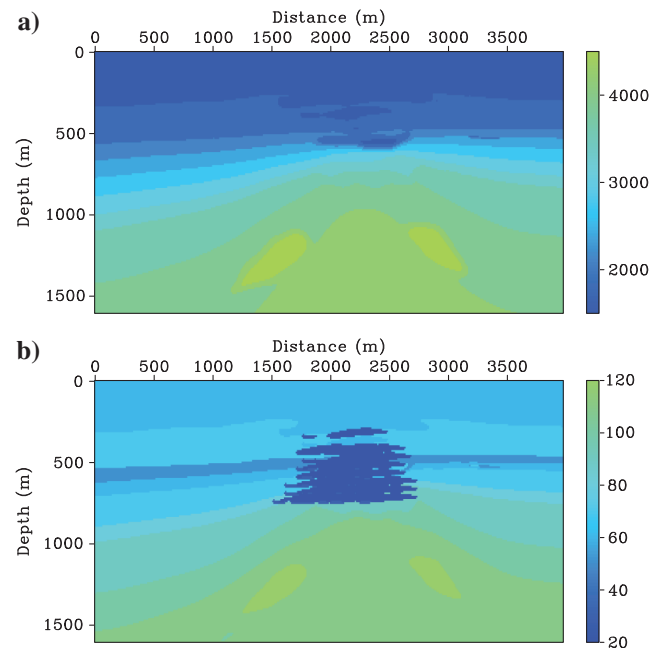

Figure 14. (a) Velocity and (b) *Q* of the BP gas chimney model, which contains a high-attenuation gas chimney exhibiting an extreme attenuating property with $Q = 20$.

For a clearer comparison, we display magnified seismic images in Figure 21 corresponding to Figures 15a and 20, in which we select three local reflections: reflection *A* is located at the gas-bearing area, reflection *B* is the top interface of the anticline, and reflection *C* is the bulge located over the right wing of the anticline. Compared with the acoustic image in Figure 21g, the reflections shown in Figure 21a and 21b are severely under-compensated because the relatively low cut-off frequency and large stabilization factor are chosen for regularizing *Q*-RTM. Figure 21c and 21d shows local

images obtained by *Q*-RTM with a moderate cut-off frequency and stabilization factor. Compared with the images of conventional filtered *Q*-RTM, our proposed *Q*-RTM tends to more fully recover the reflection amplitudes and to maintain a higher S/N, particularly the anticline structure beneath the gas chimney zone (reflection *B*). We further select a relatively higher cut-off frequency of 90 Hz and a smaller stabilization factor of 0.0025% for *Q*-RTM, Figure 21e and 21f shows the over-compensated reflections in the gas chimney, which are flooded by boosted artifacts resulting from amplitude compensation, but comparatively speaking, the adaptive stabilized *Q*-RTM image seems to have better amplitude preservation and higher quality of continuity when we compare reflections *A* and *B* in Figure 21e with those in Figure 21f. Altogether, we can conclude that *Q*-RTM using our proposed stabilization scheme tends to keep a better balance between fidelity and stability due to its superior property of time variance and *Q* dependence.
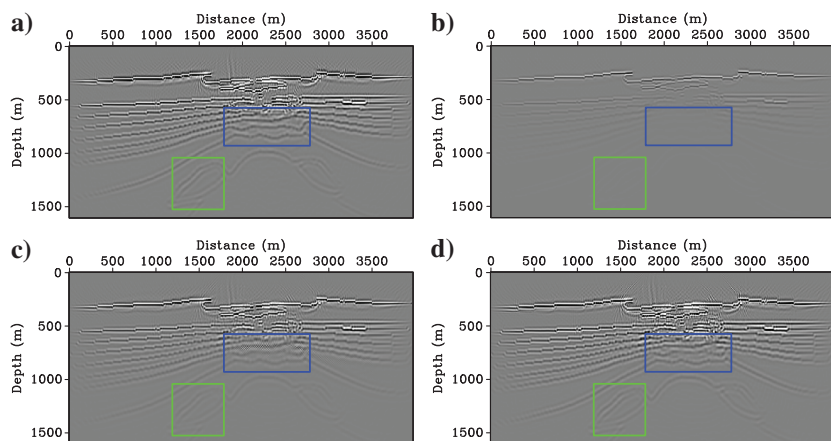

Figure 15. Migrated images obtained using (a) acoustic RTM, (b) viscoacoustic RTM without compensation, (c) low-pass-filtered *Q*-RTM, and (d) adaptively stabilized *Q*-RTM. The blue and green frames highlight migration results of the gas chimney and the bulge, respectively.

DISCUSSION

Amplitude absorption and phase distortion caused by the anelasticity of media are the two main factors that affect structure imaging and horizon interpretation in attenuating regions, and they eventually degrade the quality of the migrated images and the reliability of the subsequent interpretation (Wang, 2009; Zhang et al., 2012; Zhu et al., 2014). On the one hand, the dissipation
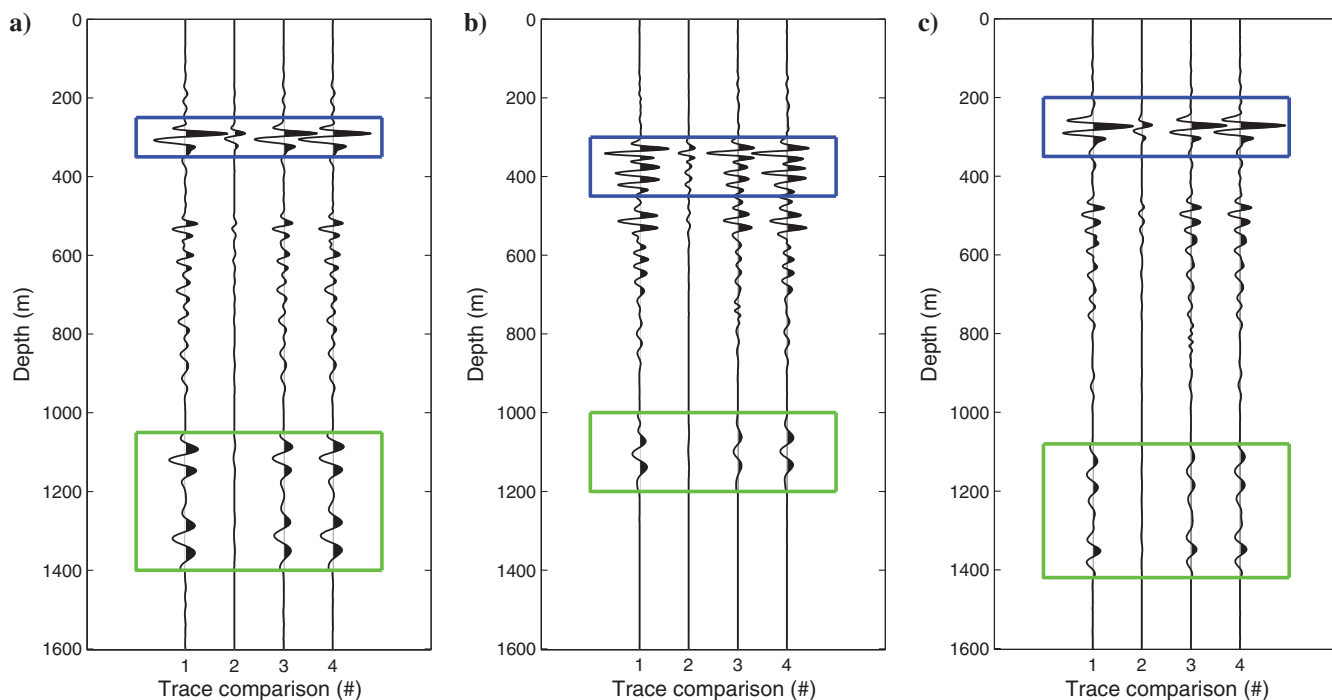

Figure 16. Migrated seismic traces selected arbitrarily at three distances of (a) 1500, (b) 2200, and (c) 3200 m from migration results shown in Figure 15. Traces 1–4 correspond to the results of acoustic RTM, viscoacoustic RTM, and *Q*-RTM using low-pass filtering and adaptive stabilization, respectively. The blue frames display the shallow structures, whereas the green frames highlighting the deep structures are shown with a gain of 10.

of seismic energy can sometimes weaken seismic waveforms, obscuring seismic events, especially the deep structure beneath high-attenuating zone; on the other hand, the accompanying phase distortion and polarity diversification may result in dislocation of events, hindering
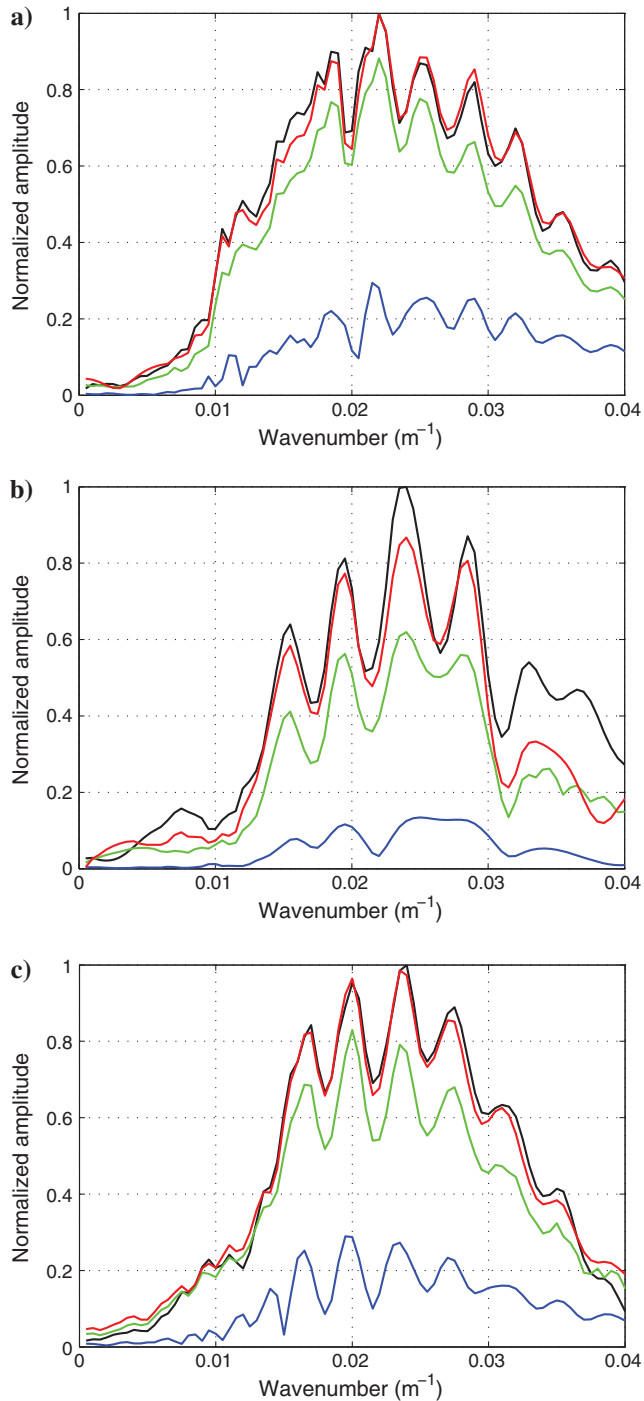
accurate seismic horizon calibration (Carcione, 2007; Wang, 2009). There are more and more seismic data processing and imaging methods aiming at compensating for attenuation effects, increasing spatial resolution of seismic images, and improving the fidelity of the reflection amplitude. The most commonly used methods include inverse-*Q* filtering (Hargreaves and Calvert, 1991; Wang, 2002, 2006), inverse-*Q* migration (Dai and West, 1994; Zhang et al., 2012), and the most recent *Q*-RTM (Zhang et al., 2010; Zhu et al., 2014; Guo et al., 2016; Li et al., 2016b; Sun et al., 2016).

A common issue existing in the compensation approaches mentioned above is the numerical instability. It has been stated in the literature that direct amplitude compensation will inevitably result in exponentially boosted high-frequency ambient noise (Wang, 2002; Zhu et al., 2014; Sun and Zhu, 2015). In this paper, we have analytically proven that the compensated constant-*Q* equation is a heavily ill-posed equation due to the presence of the compensating term. Here, we intend to give a thorough discussion about the stability and feasibility of several stabilization schemes for *Q*-RTM. The most intuitive method is to apply a Tukey window to the amplitude compensation operator in the wavenumber domain, which maintains the fidelity of compensated images within the filter pass band and serves as a time-invariant low-pass filter suppressing high-frequency noise (Treeby et al., 2010; Zhu et al., 2014). Inspired by the fact that signal loss manifests as a depth-dependent magnitude decrease and blurring of features within the recorded data, Treeby (2013) proposes a regularization scheme by using a time-variant window, in which the cut-

Figure 17. Amplitude spectra corresponding to the migrated seismic traces shown in Figure 16 at three distances of (a) 1500, (b) 2200, and (c) 3200 m, where the black line stands for the amplitude spectrum of acoustic trace 1, the blue line stands for that of attenuated trace 2, and the green and red lines stand for that of compensated traces 3 and 4, respectively.
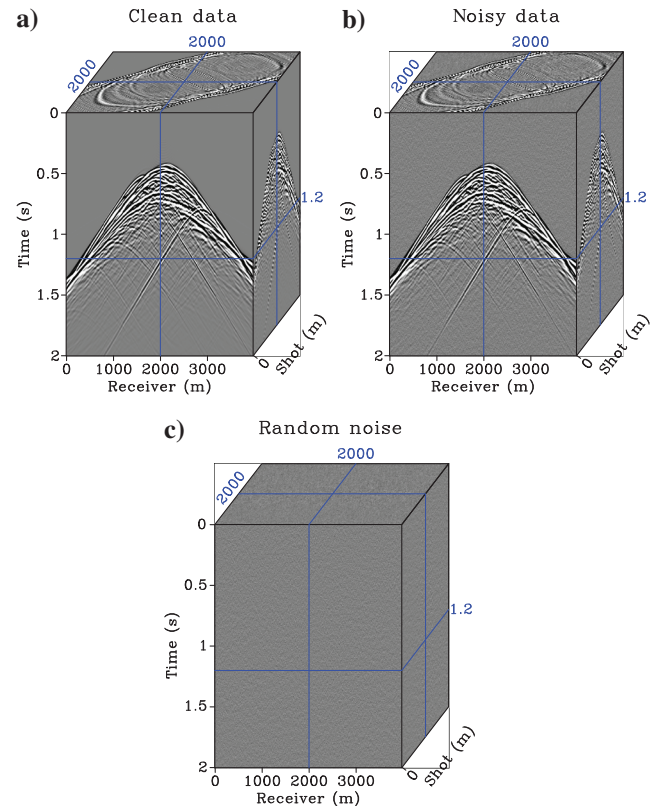

Figure 18. (a) Synthesized data from the BP gas chimney model, (b) synthesized data added five band-pass filtered random noise, and (c) band-pass filtered random noise. We clip the same amplitude value for all three figures.
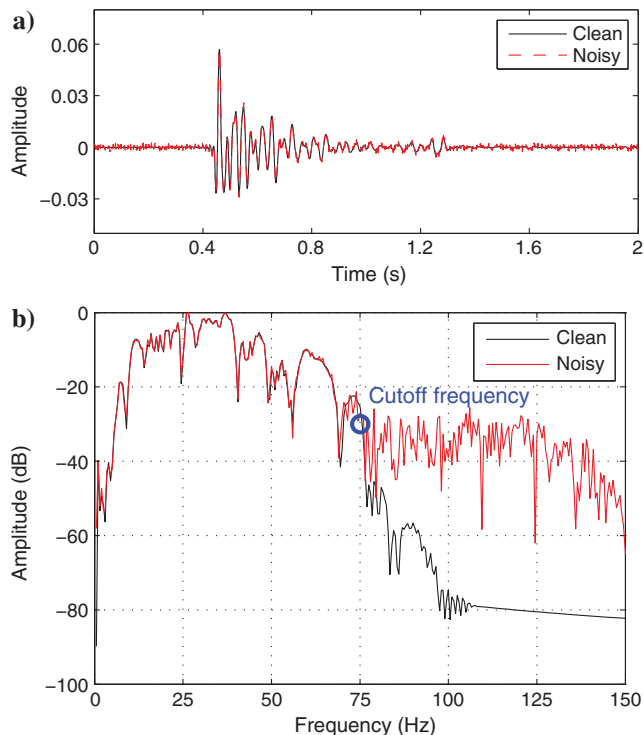
Figure 19. (a) Synthetic traces selected arbitrarily at a distance of 2000 m from shot 40 of seismic records shown in Figure 18: The black line corresponds to the clean data, and the red line to noisy data. (b) Amplitude spectra corresponding to the synthetic traces shown in Figure 19a.
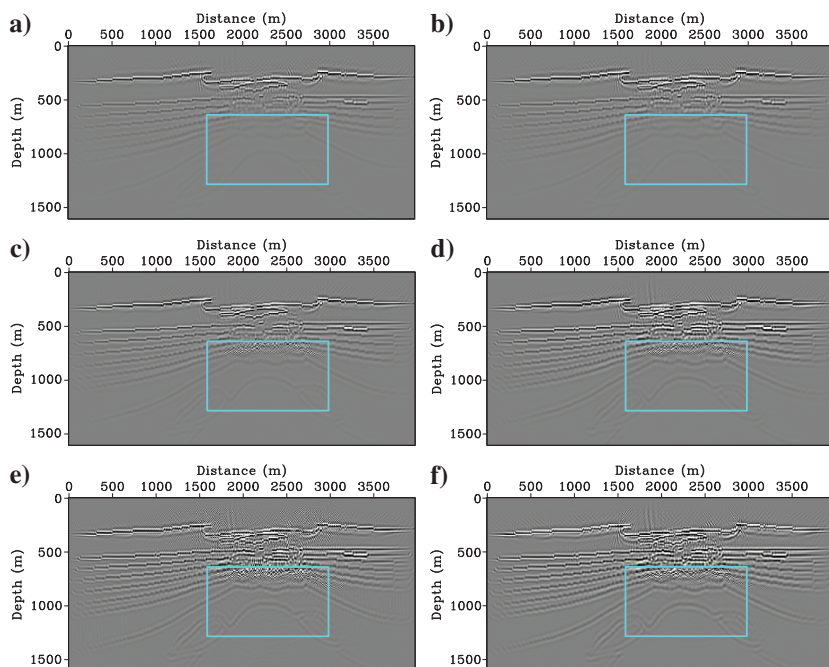

Figure 20. Migrated images from the noisy data with 5% random noise obtained using low-pass-filtered Q-RTM with three different cut-off frequencies (a) $\rho = 60$, (c) 75, and (e) 90 Hz, and our proposed Q-RTM with three different stabilization factors (b) $\sigma^2 = 0.25\%$, (d) 0.025\%, and (f) 0.0025\%.

off frequency is based on the local time-frequency distribution of the recorded signals. Sun and Zhu (2015) propose a novel approach to stabilize the attenuation compensation that aims at reformulating a stable compensation operator without explicitly amplifying the wave amplitude. This stable compensation can be achieved by a smooth division between a phase-only wavefield and a viscoacoustic wavefield. However, there are two main drawbacks of this method. First, the computational cost of this method is approximately 1.5–2 times higher than that of the conventional RTMs; second, such a method avoids the instability caused by exponentially amplifying the attenuated data, meanwhile bringing in another instability problem of division by zero. Even though smooth division by shaping regularization is performed (Fomel, 2007; Chen et al., 2014, 2017; Xue et al., 2015), it is hard to guarantee the fidelity of the result in a complex structure region. An alternative attempt is to stabilize the amplitude compensation by adding regularization terms (Zhang et al., 2010; Qu et al., 2015), which requires careful control on the regularization term. Besides, inversion-based compensation schemes have been widely studied by many researchers (Blanch and Symes, 1995; Ribodetti et al., 1995; Dutta and Schuster, 2014; Sun et al., 2016). Ribodetti et al. (1995) develop an inversion scheme in the frequency domain for recovering the three spatially dependent parameters of a viscoacoustic medium. Later, they generalize this theory for viscoelastic seismic imaging (Ribodetti and Virieux, 1998). Blanch and Symes (1995) propose an efficient iterative viscoacoustic linearized inversion strategy based on the SLS model. Recently, Dutta and Schuster (2014) and Sun et al. (2016) propose Q-compensated least-squares RTM (Q-LSRTM) based on the SLS viscoacoustic-wave equation and constant-Q wave equation, respectively. They claim that attenuation compensation in the framework of LSRTM is always stable without making any modification or regularization upon the adjoint wave equations during the backward wavefield extrapolation. In this sense, Q-LSRTM is a promising way for removing the side effects of attenuation to seismic imaging. In summary, the stabilization scheme proposed in this paper can be treated as a nonstationary filtering method that exhibits the superior property of time variance and Q dependence over conventional low-pass filtering.

Another issue that we should pay attention to is the choice of stabilization parameter, which is the key to maintain a successful and stable compensation. As we all know, the stability of source and receiver wavefield compensation is not only determined by the physical properties of subsurface media (velocity and Q models) but also by input data (source and seismic records). As a result, the cut-off wavenumber or the stabilization factor in Q-RTM is physically linked to the noise level of the source and seismic records. Furthermore, it is more reasonable to select distinct stabilization parameters for source and receiver wavefield extrapolation because the S/N of the forward wavefield is typically much higher than that of measured seismic records. However, conventional low-pass filtering is somehow a rough approach when compared with our proposed stabilization scheme.

Although our proposed stabilization scheme exhibits the superior properties of time-variance and *Q*-dependence over conventional low-pass filtering, it is still a nonlocal operator acting on the wavenumber-domain wavefields and is independent of space locations. As we can see from Figure 20, the boosted ambient noise caused by amplitude compensation mainly distributes around the high-attenuation gas chimney area, which indicates that a space-dependent stabilization operator $\Lambda(\mathbf{k}, \mathbf{x}, t)$ might be the optimal choice. Such a mixed-domain space-wavenumber operator can be formulated by space-wavenumber analysis (Stockwell et al., 2006; Pai and Sundaresan, 2011), and further simulated using low-rank decomposition (Fomel et al., 2013; Song et al., 2013; Sun et al., 2016). An alternative approach to establish the inherent relation between spatial state and wavenumber-domain state is empirical-mode decomposition (EMD) (Huang et al., 1998; Huang and Wu, 2008), by which one can conduct stabilization in the space and wavenumber domain simultaneously. The beauty of the EMD-based method is that EMD is a local and fully adaptive method that can be used to attenuate the highly oscillating spatial components (high-wavenumber components) without any input parameter. Once an appropriate spatiotemporal stabilization operator is proposed, it will be a promising candidate for many adjoint-state-based compensation methods (Plessix, 2006), including *Q*-RTM (Zhang et al., 2010; Zhu et al., 2014; Guo et al., 2016; Li et al., 2016b; Sun et al., 2016), viscoelastic time-reversal reconstruction and imaging (Zhu, 2014; Wang et al., 2017b), and possible *Q*-FWI (Ren et al., 2014; Xue et al., 2016; Xue et al., 2016; Yang et al., 2016a). This challenging open problem will be our future work.

Finally, we would like to have a brief discussion on possible errors of the proposed adaptive stabilization scheme. It is regrettable that accuracy and stability are usually opposite each other; what we need to do is to make a reasonable trade-off between them. As we can see from Figure 7, our proposed method recovers as many high-wavenumber components of the shallow structure as possible compared with that of low-pass filtering, and it obtains comparable accuracy with the filtering scheme at a medium propagation time. After a relatively long traveltime, our method might generate inaccurate results because of much more severe medium- and high-wavenumber suppression, but our method enjoys better stability during amplitude compensation for deep reflectors. A pre-estimated range of the cut-off wavenumber might be beneficial to reach a balance between accuracy and stability. Alternatively, we can make the cut-off wavenumber of the proposed adaptive stabilization scheme converge to a constant wavenumber as the filtering method does during long-time extrapolation, avoiding the unacceptable errors resulting from severe high-wavenumber suppression. We will pay much more attention to improving accuracy and stability of the proposed method in our future research.

CONCLUSION

We have analytically derived *k*-space Green's functions for decoupled constant-*Q* wave equation and its compensated equation. It is an exponentially divergent time propagator of the Green's function that will result in numerical instability during attenuation compensation. Based upon theoretical analysis, we have developed an adaptive stabilization scheme for *Q*-RTM, in which the stabilization factor can be explicitly identified by the specified gain limit according to an empirical formula. In comparison with conventional low-pass filtering, our proposed stabilization scheme exhibits superior properties of time variance and *Q* dependence. Noise-free *Q*-RTM using low-pass filtering and adaptive stabilization have been performed on a simple five-layer model and the BP gas chimney model for verifying the superiority of the proposed approach in terms of fidelity and stability. We have also conducted stabilized *Q*-RTM for the BP gas chimney model with noisy data, which further demonstrates that our proposed method brings better antinoise performance and slight resolution enhancement.
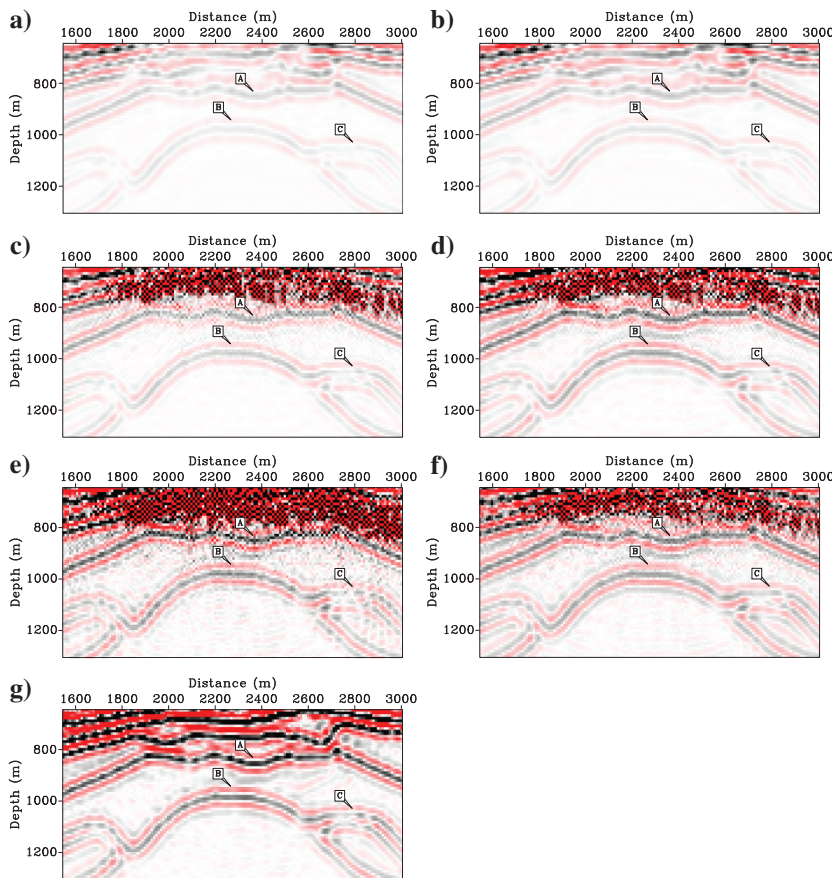

Figure 21. (a-f) Magnified view of the images shown in Figure 20 and (g) magnified view of acoustic image shown in Figure 15a.

ACKNOWLEDGMENTS

APPENDIX A

ANALYTICAL INTEGRATION USING CAUCHY'S RESIDUE THEOREM

In this appendix, we outline the analytical integration using Cauchy's residue theorem in detail (Mitrinovic and Keckic, 1984). As we can see from equation 14, the kernel function $h(\mathbf{k}, \omega)$ has two singularities located in the upper half-space of the complex plane (Figure A-1). Here, we adopt the following approach proposed by Treeby and Cox (2011) to solve the integration with respect to ω. Cauchy's residue theorem is considered as a powerful tool to evaluate line integrals of analytic functions over closed curves. For simplicity, we rewrite the kernel function $h(\mathbf{k}, \omega)$ as

$$f(\zeta) = \frac{e^{i\zeta(t-t_0)}}{\zeta^2 + i\tau|\mathbf{k}|^{2\gamma+1}c^2\zeta + \eta|\mathbf{k}|^{2\gamma+2}c^2}. \quad (A-1)$$

Setting $t_0 = 0$ without loss of generality, and the contour C may be split into a straight part and a curved arc, so that the integration can be expressed as

$$\oint_C f(\zeta)d\zeta = \int_{C_{\text{straight}}} f(\zeta)d\zeta + \int_{C_{\text{arc}}} f(\zeta)d\zeta,$$
$$= -2\pi i\{\text{Res}[f(\zeta), \zeta_1] + \text{Res}[f(\zeta), \zeta_2]\},$$
$$= -2\pi i\left(\frac{e^{i\xi_1 t}e^{-\xi_2 t}}{2\xi_1} + \frac{e^{-i\xi_1 t}e^{-\xi_2 t}}{-2\xi_1}\right),$$
$$= 2\pi \frac{\sin(\xi_1 t)e^{-\xi_2 t}}{\xi_1}, \quad (A-2)$$

where ζ_1 and ζ_2 are the two poles of kernel function $h(\mathbf{k}, \omega)$, which are given in equation 16. Our goal is to solve the integration of the kernel function $h(\mathbf{k}, \omega)$ with respect to ω, where
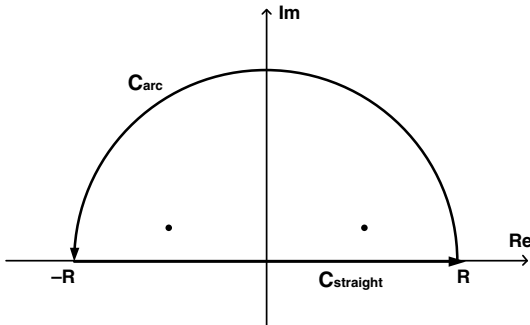

Figure A-1. Integration of the kernel function $h(\mathbf{k}, \omega)$ over the contour C using Cauchy's residue theorem.

$$\int h(\mathbf{k}, \omega)d\omega = \lim_{R \to \infty}\left[\int_{-R}^{R} f(\zeta)d\zeta\right],$$
$$= \oint_C f(\zeta)d\zeta - \lim_{R \to \infty}\left[\int_{C_{\text{arc}}} f(\zeta)d\zeta\right]. \quad (A-3)$$

Therefore, we need to calculate the contour integral $\lim_{R \to \infty}\left[\int_{C_{\text{arc}}} f(\zeta)d\zeta\right]$. The estimation lemma is also known as the ML inequality, gives an upper bound for a contour integral (Saff and Snider, 1976). The statement is as follows:

LEMMA 1

If $f(z)$ is a complex-valued, continuous function on the contour C_{arc} and if its absolute value $|f(z)|$ is bounded by a constant M for all z on C_{arc}, then

$$\left|\int_{C_{\text{arc}}} f(z)dz\right| \leq Ml(C_{\text{arc}}),$$

where $l(C_{\text{arc}})$ is the arc length of C_{arc}.

According to Lemma 1, we can obtain the following inequality:

$$\left|\int_{C_{\text{arc}}} \frac{e^{i\zeta t}}{\zeta^2 + i\tau|\mathbf{k}|^{2\gamma+1}c^2\zeta + \eta|\mathbf{k}|^{2\gamma+2}c^2}d\zeta\right|$$
$$\leq \int_{C_{\text{arc}}} \left|\frac{e^{i\zeta t}}{\zeta^2 + i\tau|\mathbf{k}|^{2\gamma+1}c^2\zeta + \eta|\mathbf{k}|^{2\gamma+2}c^2}\right|d\zeta,$$
$$\leq \int_{C_{\text{arc}}} \frac{1}{|\zeta^2 + i\tau|\mathbf{k}|^{2\gamma+1}c^2\zeta + \eta|\mathbf{k}|^{2\gamma+2}c^2|}d\zeta,$$
$$\leq \int_{C_{\text{arc}}} \frac{1}{R^2 + \eta|\mathbf{k}|^{2\gamma+2}c^2}d\zeta = \frac{\pi R}{R^2 + \eta|\mathbf{k}|^{2\gamma+2}c^2}. \quad (A-4)$$

Note that, because $t > 0$ and for complex numbers in the upper half-plane, the argument lies between 0 and π, one can estimate

$$|e^{i\zeta t}| = |e^{it|\zeta|(\cos \phi + i \sin \phi)}| = e^{-t|\zeta|\sin \phi} \leq 1. \quad (A-5)$$

Therefore,

$$\int_{C_{\text{arc}}} \left|\frac{e^{i\zeta t}}{\zeta^2 + i\tau|\mathbf{k}|^{2\gamma+1}c^2\zeta + \eta|\mathbf{k}|^{2\gamma+2}c^2}\right|d\zeta$$
$$\leq \int_{C_{\text{arc}}} \frac{1}{|\zeta^2 + i\tau|\mathbf{k}|^{2\gamma+1}c^2\zeta + \eta|\mathbf{k}|^{2\gamma+2}c^2|}d\zeta. \quad (A-6)$$

Next, we seek an upper bound M for the integrand when $|\zeta| = R$; here, we denote complex-valued function:

$$g(\zeta) = \zeta^2 + i\tau|\mathbf{k}|^{2\gamma+1}c^2\zeta + \eta|\mathbf{k}|^{2\gamma+2}c^2, \quad (A-7)$$

which can be projected on the real plane as the following real-valued function:

$$q(\nu) = \nu^2 + \eta|\mathbf{k}|^{2\gamma+2}c^2, \quad (A-8)$$

where ν is the real part of ζ, and $\eta|\mathbf{k}|^{2\gamma+2}c^2$ can be estimated by using the Vieta's theorem

$$\eta|\mathbf{k}|^{2\gamma+2}c^2 = \zeta_1 \cdot \zeta_2 > -R^2. \quad (A-9)$$

By the triangle inequality, we see that

$$|g(\zeta)| = |q(R)| = |R^2 + \eta|\mathbf{k}|^{2\gamma+2}c^2| \geq R^2 + \eta|\mathbf{k}|^{2\gamma+2}c^2 > 0. \tag{A-10}$$

Therefore,

$$\int_{C_{\mathrm{arc}}} \frac{1}{|\zeta^2 + i\tau|\mathbf{k}|^{2\gamma+1}c^2\zeta + \eta|\mathbf{k}|^{2\gamma+2}c^2|} \, d\zeta$$
$$\leq \int_{C_{\mathrm{arc}}} \frac{1}{R^2 + \eta|\mathbf{k}|^{2\gamma+2}c^2} \, d\zeta. \tag{A-11}$$

According to equation A-4, we have

$$\lim_{R\to\infty}\left[\int_{C_{\mathrm{arc}}} f(\zeta)d\zeta\right] \leq \lim_{R\to\infty} \frac{\pi R}{R^2 + \eta|\mathbf{k}|^{2\gamma+2}c^2} = 0. \tag{A-12}$$

Therefore, the arc integration $\int_{C_{\mathrm{arc}}} f(\zeta)d\zeta \to 0$ when $R \to \infty$, and hence

$$\int h(\mathbf{k},\omega)d\omega = \oint_C f(\zeta)d\zeta - \lim_{R\to\infty}\left[\int_{C_{\mathrm{arc}}} f(\zeta)d\zeta\right],$$
$$= 2\pi\frac{\sin(\xi_1 t)e^{-\xi_2 t}}{\xi_1}. \tag{A-13}$$

REFERENCES

Ammari, H., 2008, An introduction to mathematics of emerging biomedical imaging: Springer.

Ammari, H., E. Bretin, J. Garnier, and A. Wahab, 2013, Time reversal algorithms in viscoelastic media: European Journal of Applied Mathematics, **24**, 565–600, doi: 10.1017/S0956792513000107.

Bai, M., X. Chen, J. Wu, Y. Chen, G. Liu, and E. Wang, 2016a, Multiple-component Gaussian beam reverse-time migration based on attenuation compensation: Chinese Journal of Geophysics-Chinese Edition, **59**, 3379–3393.

Bai, M., X. Chen, J. Wu, G. Liu, Y. Chen, H. Chen, and Q. Li, 2016b, Q-compensated migration by Gaussian beam summation method: Journal of Geophysics and Engineering, **13**, 35–48, doi: 10.1088/1742-2132/13/1/35.

Berkhout, A. J., 2012, Seismic migration: Imaging of acoustic energy by wavefield extrapolation: Elsevier.

Blanch, J. O., and W. W. Symes, 1995, Efficient iterative viscoacoustic linearized inversion: 65th Annual International Meeting, SEG, Expanded Abstracts, 627–630.

Carcione, J. M., 2007, Wave fields in real media: Wave propagation in anisotropic, anelastic, porous, and electromagnetic media: Elsevier.

Carcione, J. M., 2008, Theory and modeling of constant-*Q* P-and S-waves using fractional time derivatives: Geophysics, **74**, no. 1, T1–T11, doi: 10.1190/1.3008548.

Carcione, J. M., 2010, A generalization of the Fourier pseudospectral method: Geophysics, **75**, no. 6, A53–A56, doi: 10.1190/1.3509472.

Carcione, J. M., F. Cavallini, F. Mainardi, and A. Hanyga, 2002, Time-domain modeling of constant-*Q* seismic waves using fractional derivatives: Pure and Applied Geophysics, **159**, 1719–1736, doi: 10.1007/s00024-002-8705-z.

Carcione, J. M., D. Kosloff, and R. Kosloff, 1988, Wave propagation simulation in a linear viscoelastic medium: Geophysical Journal International, **93**, 393–401, doi: 10.1111/j.1365-246X.1988.tb02010.x.

Chen, H., H. Zhou, Q. Li, and Y. Wang, 2016, Two efficient modeling schemes for fractional Laplacian viscoacoustic wave equation: Geophysics, **81**, no. 5, T233–T249, doi: 10.1190/geo2015-0660.1.

Chen, Y., H. Chen, K. Xiang, and X. Chen, 2017, Preserving the discontinuities in least-squares reverse time migration of simultaneous-source data: Geophysics, **82**, no. 3, S185–S196, doi: 10.1190/geo2016-0456.1.

Chen, Y., S. Fomel, and J. Hu, 2014, Iterative deblending of simultaneous-source seismic data using seislet-domain shaping regularization: Geophysics, **79**, no. 5, V179–V189, doi: 10.1190/geo2013-0449.1.

Clarke, G. K., 1968, Time-varying deconvolution filters: Geophysics, **33**, 936–944, doi: 10.1190/1.1439987.

Dai, N., and G. F. West, 1994, Inverse Q migration: 64th Annual International Meeting, SEG, Expanded Abstracts, 1418–1421.

Dutta, G., and G. T. Schuster, 2014, Attenuation compensation for least-squares reverse time migration using the viscoacoustic-wave equation: Geophysics, **79**, no. 6, S251–S262, doi: 10.1190/geo2013-0414.1.

Fomel, S., 2007, Shaping regularization in geophysical-estimation problems: Geophysics, **72**, no. 2, R29–R36, doi: 10.1190/1.2433716.

Fomel, S., L. Ying, and X. Song, 2013, Seismic wave extrapolation using lowrank symbol approximation: Geophysical Prospecting, **61**, 526–536, doi: 10.1111/j.1365-2478.2012.01064.x.

Griffiths, L., F. Smolka, and L. Trembly, 1977, Adaptive deconvolution: A new technique for processing time-varying seismic data: Geophysics, **42**, 742–759, doi: 10.1190/1.1440743.

Guo, P., and G. A. Mcmechan, 2015, Separation of absorption and dispersion effects in *Q*-compensated viscoelastic RTM: 85th Annual International Meeting, SEG, Expanded Abstracts, 3966–3971.

Guo, P., G. A. McMechan, and H. Guan, 2016, Comparison of two viscoacoustic propagators for Q-compensated reverse time migration: Geophysics, **81**, no. 5, S281–S297, doi: 10.1190/geo2015-0557.1.

Hargreaves, N. D., and A. J. Calvert, 1991, Inverse *Q* filtering by Fourier transform: Geophysics, **56**, 519–527, doi: 10.1190/1.1443067.

Holm, S., and S. P. Nsholm, 2014, Comparison of fractional wave equations for power law attenuation in ultrasound and elastography: Ultrasound in Medicine & Biology, **40**, 695–703, doi: 10.1016/j.ultrasmedbio.2013.09.033.

Huang, C., L. Nie, R. W. Schoonover, L. V. Wang, and M. A. Anastasio, 2012, Photoacoustic computed tomography correcting for heterogeneity and attenuation: Journal of Biomedical Optics, **17**, 318–321, doi: 10.1117/1.JBO.17.6.061211.

Huang, N. E., Z. Shen, S. R. Long, M. C. Wu, H. H. Shih, Q. Zheng, N. C. Yen, C. T. Chi, and H. H. Liu, 1998, The empirical mode decomposition and the Hilbert spectrum for nonlinear and non-stationary time series analysis: Proceedings of the Royal Society A: Mathematical Physical & Engineering Sciences, **454**, 903–995, doi: 10.1098/rspa.1998.0193.

Huang, N. E., and Z. Wu, 2008, A review on Hilbert-Huang transform: Method and its applications to geophysical studies: Reviews of Geophysics, **46**, RG2006, doi: 10.1029/2007RG000228.

Irving, J. D., and R. J. Knight, 2003, Removal of wavelet dispersion from ground-penetrating radar data: Geophysics, **68**, 960–970, doi: 10.1190/1.1581068.

Kalimeris, K., and O. Scherzer, 2013, Photoacoustic imaging in attenuating acoustic media based on strongly causal models: Mathematical Methods in the Applied Sciences, **36**, 2254–2264, doi: 10.1002/mma.v36.16.

Kelly, J. F., R. J. Mcgough, and M. M. Meerschaert, 2008, Analytical time-domain Green's functions for power-law media: Journal of the Acoustical Society of America, **124**, 2861–2872, doi: 10.1121/1.2977669.

Kjartansson, E., 1979, Constant *Q*-wave propagation and attenuation: Journal of Geophysical Research Solid Earth, **84**, 4737–4748, doi: 10.1029/JB084iB09p04737.

Li, G., M. D. Sacchi, and H. Zheng, 2016a, In situ evidence for frequency dependence of near-surface Q: Geophysical Journal International, **204**, 1308–1315, doi: 10.1093/gji/ggv523.

Li, Q., H. Zhou, Q. Zhang, H. Chen, and S. Sheng, 2016b, Efficient reverse time migration based on fractional Laplacian viscoacoustic wave equation: Geophysical Journal International, **204**, 488–504, doi: 10.1093/gji/ggv456.

Liu, H., D. L. Anderson, and H. Kanamori, 1976, Velocity dispersion due to anelasticity: Implications for seismology and mantle composition: Geophysical Journal International, **47**, 41–58, doi: 10.1111/j.1365-246X.1976.tb01261.x.

Margrave, G. F., M. P. Lamoureux, and D. C. Henley, 2011, Gabor deconvolution: Estimating reflectivity by nonstationary deconvolution of seismic data: Geophysics, **76**, no. 3, W15–W30, doi: 10.1190/1.3560167.

McDonal, F., F. Angona, R. Mills, R. Sengbush, R. Van Nostrand, and J. White, 1958, Attenuation of shear and compressional waves in Pierre shale: Geophysics, **23**, 421–439, doi: 10.1190/1.1438489.

Mitrinovic, D. S., and J. D. Keckic, 1984, The Cauchy method of residues: Theory and applications: Springer Science & Business Media.

Mittet, R., 2007, A simple design procedure for depth extrapolation operators that compensate for absorption and dispersion: Geophysics, **72**, no. 2, S105–S112, doi: 10.1190/1.2431637.

Mittet, R., R. Sollie, and K. Hokstad, 1995, Prestack depth migration with compensation for absorption and dispersion: Geophysics, **60**, 1485–1494, doi: 10.1190/1.1443882.

Pai, P. F., and M. J. Sundaresan, 2011, Time-frequency and space-wavenumber analysis for damage inspection of thin-walled structures: SPIE Smart Structures and Materials+ Nondestructive Evaluation and Health Monitoring, International Society for Optics and Photonics, 79842J.

Plessix, R. E., 2006, A review of the adjoint-state method for computing the gradient of a functional with geophysical applications: Geophysical

Journal International, **167**, 495–503, doi: 10.1111/j.1365-246X.2006 .02978.x.

Qu, Y., Z. Li, J. Huang, W. Deng, and J. Li, 2015, The application of pseudospectral method and a stable reverse-time propagator for viscoacoustic RTM: 85th Annual International Meeting, SEG, Expanded Abstracts, 4355–4359.

Ren, Z., Y. Liu, and Q. Zhang, 2014, Multiscale viscoacoustic waveform inversion with the second generation wavelet transform and adaptive timespace domain finite-difference method: Geophysical Journal International, **197**, 948–974, doi: 10.1093/gji/ggu024.

Ribodetti, A., and J. Virieux, 1998, Asymptotic theory for imaging the attenuation factors QP and QS: Social Science Electronic Publishing, 747.

Ribodetti, A., J. Virieux, and S. Durand, 1995, Asymptotic theory for viscoacoustic seismic imaging: 65th Annual International Meeting, SEG, Expanded Abstracts, 631–634.

Saff, E. B., and A. D. Snider, 1976, Fundamentals of complex analysis for mathematics, science, and engineering: Prentice-Hall.

Song, X., S. Fomel, and L. Ying, 2013, Lowrank finite-differences and lowrank fourier finite-differences for seismic wave extrapolation in the acoustic approximation: Geophysical Journal International, **193**, 960–969, doi: 10.1093/gji/ggt017.

Stockwell, R., M. J. Taylor, K. Nielsen, and M. Jarvis, 2006, A novel joint space-wavenumber analysis of an unusual antarctic gravity wave event: Geophysical Research Letters, **33**, L08805, doi: 10.1029/2005GL025660.

Sun, J., S. Fomel, T. Zhu, and J. Hu, 2016, Q-compensated least-squares reverse time migration using low-rank one-step wave extrapolation: Geophysics, **81**, no. 4, S271–S279, doi: 10.1190/geo2015-0520.1.

Sun, J., and T. Zhu, 2015, Stable attenuation compensation in reverse-time migration: 85th Annual International Meeting, SEG, Expanded Abstracts, 3942–3947.

Sun, J., T. Zhu, and S. Fomel, 2014, Viscoacoustic modeling and imaging using low-rank approximation: Geophysics, **80**, no. 5, A103–A108, doi: 10.1190/geo2015-0083.1.

Treeby, B. E., 2013, Acoustic attenuation compensation in photoacoustic tomography using time-variant filtering: Journal of Biomedical Optics, **18**, 036008, doi: 10.1117/1.JBO.18.3.036008.

Treeby, B. E., and B. T. Cox, 2010, Modeling power law absorption and dispersion for acoustic propagation using the fractional Laplacian: Journal of the Acoustical Society of America, **127**, 2741–2748, doi: 10.1121/1 .3377056.

Treeby, B. E., and B. Cox, 2011, A k-space green's function solution for acoustic initial value problems in homogeneous media with power law absorption: The Journal of the Acoustical Society of America, **129**, 3652–3660, doi: 10.1121/1.3583537.

Treeby, B. E., E. Z. Zhang, and B. T. Cox, 2010, Photoacoustic tomography in absorbing acoustic media using time reversal: Inverse Problems, **26**, 115003–115020, doi: 10.1088/0266-5611/26/11/115003.

Wang, S., X. Li, B. Di, and B. David, 2010, Reservoir fluid substitution effects on seismic profile interpretation: A physical modeling experiment: Geophysical Research Letters, **37**, 198–209, doi: 10.1029/2010GL043090.

Wang, S., X. Y. Li, Z. Qian, B. Di, and J. Wei, 2007, Physical modeling studies of 3-D P-wave seismic for fracture detection: Geophysical Journal International, **168**, 745–756, doi: 10.1111/j.1365-246X.2006.03215.x.

Wang, Y., 2002, A stable and efficient approach of inverse Q filtering: Geophysics, **67**, 657–663, doi: 10.1190/1.1468627.

Wang, Y., 2006, Inverse Q-filter for seismic resolution enhancement: Geophysics, **71**, no. 3, V51–V60, doi: 10.1190/1.2192912.

Wang, Y., 2009, Seismic inverse Q filtering: John Wiley & Sons.

Wang, Y., and J. Guo, 2004, Seismic migration with inverse Q filtering: Geophysical Research Letters, **31**, 163–183, doi: 10.1029/2003GL018323.

Wang, Y., H. Zhou, Q. Li, H. Chen, S. Gan, and Y. Chen, 2015, An unsplit convolutional perfectly matched layer for visco-acoustic wave equation with fractional time derivatives: 85th Annual International Meeting, SEG, Expanded Abstracts, 3666–3671.

Wang, Y., H. Zhou, Q. Li, X. Zhao, X. Zhao, and Y. An, 2017a, Regularized Q-RTM using time-variant filtering in the k-space: 79th Annual International Conference and Exhibition, EAGE, Extended Abstracts, doi: 10.3997/2214-4609.201700676.

Wang, Y., H. Zhou, Q. Zhang, X. Zhao, Z. Zhou, and Y. An, 2017b, Wavefield reconstruction in attenuating media using time-reversal checkpointing and k-space filtering: 79th Annual International Conference and Exhibition, EAGE, Extended Abstracts, doi: 10.3997/2214-4609 .201701152.

Wang, Y., H. Zhou, X. Zhao, M. Xia, and X. Cai, 2017c, The k-space Greens functions for decoupled constant-Q wave equation and its adjoint equation: 79th Annual International Conference and Exhibition, EAGE, Extended Abstracts, doi: 10.3997/2214-4609.201701153.

Wuenschel, P. C., 1965, Dispersive body waves: An experimental study: Geophysics, **30**, 539–551, doi: 10.1190/1.1439620.

Xue, Z., T. Zhu, S. Fomel, and J. Sun, 2016, Q-compensated full-waveform inversion using constant-q wave equation: 86th Annual International Meeting, SEG, Expanded Abstracts, 1063–1068.

Xue, Z., N. Alger, and S. Fomel, 2016, Full-waveform inversion using smoothing kernels: 86th Annual International Meeting, SEG, Expanded Abstracts, 1358–1363.

Xue, Z., Y. Chen, S. Fomel, and J. Sun, 2015, Seismic imaging of incomplete data and simultaneous-source data using least-squares reverse time migration with shaping regularization: Geophysics, **81**, no. 1, S11–S20, doi: 10.1190/geo2014-0524.1.

Yang, P., R. Brossier, L. Métivier, and J. Virieux, 2016a, A review on the systematic formulation of 3-D multiparameter full waveform inversion in viscoelastic medium: Geophysical Journal International, **207**, 129–149, doi: 10.1093/gji/ggw262.

Yang, P., R. Brossier, L. Métivier, and J. Virieux, 2016b, Wavefield reconstruction in attenuating media: A checkpointing-assisted reverse-forward simulation method: Geophysics, **81**, no. 6, R349–R362, doi: 10 .1190/geo2016-0082.1.

Yilmaz, O., 2001, Seismic data analysis: SEG.

Zhang, J., J. Wu, and X. Li, 2012, Compensation for absorption and dispersion in prestack migration: An effective Q approach: Geophysics, **78**, no. 1, S1–S14, doi: 10.1190/geo2012-0128.1.

Zhang, Y., P. Zhang, and H. Zhang, 2010, Compensating for visco-acoustic effects in reverse time migration: 80th Annual International Meeting, SEG, Expanded Abstracts, 3160–3164.

Zhu, T., 2014, Time-reverse modeling of acoustic wave propagation in attenuating media: Geophysical Journal International, **197**, 483–494, doi: 10.1093/gji/ggt519.

Zhu, T., and J. M. Carcione, 2014, Theory and modeling of constant-Q P- and S-waves using fractional spatial derivatives: Geophysical Journal International, **196**, 1787–1795, doi: 10.1093/gji/ggt483.

Zhu, T., and J. M. Harris, 2014, Modeling acoustic wave propagation in heterogeneous attenuating media using decoupled fractional Laplacians: Geophysics, **79**, no. 3, T105–T116, doi: 10.1190/geo2013-0245.1.

Zhu, T., J. M. Harris, and B. Biondi, 2014, Q-compensated reverse-time migration: Geophysics, **79**, no. 3, S77–S87, doi: 10.1190/geo2013-0344.1.